Microphysics of Snowfall Over Coastal East Antarctica Simulated by Polar WRF and Observed by Radar

É. Vignon, N. Besic, N. Jullien, J. Gehring, A. Berne

JGR Atmospheres

RESEARCH ARTICLE
10.1029/2019JD031028

Microphysics of Snowfall Over Coastal East Antarctica Simulated by Polar WRF and Observed by Radar

É. Vignon[1], **N. Besic**[1,2], **N. Jullien**[1], **J. Gehring**[1], **and A. Berne**[1]

[1]Environmental Remote Sensing Laboratory (LTE), École Polytechnique Fédérale de Lausanne (EPFL), Lausanne, Switzerland, [2]Météo-France, Toulouse, France

Key Points:
- The microphysics of Antarctic snowfall in Polar WRF is compared to radar and MASC measurements at Dumont d'Urville station
- Despite the constrained circulation, large discrepancies between microphysical schemes appear in the amount of simulated precipitation
- Shortcomings in state-of-the-art microphysical schemes are identified, particularly regarding the sublimation and aggregation processes

Supporting Information:
- Supporting Information S1

Correspondence to:
É. Vignon,
etienne.vignon@epfl.ch

Citation:
Vignon, É., Besic, N., Jullien, N., Gehring, J., & Berne, A. (2019). Microphysics of snowfall over coastal East Antarctica simulated by Polar WRF and observed by radar. *Journal of Geophysical Research: Atmospheres*, *124*, 11,452–11,476. https://doi.org/10.1029/2019JD031028

Received 16 MAY 2019
Accepted 5 OCT 2019
Accepted article online 1 NOV 2019

Abstract The current assessment of the Antarctic surface mass balance mostly relies on reanalysis products or climate model simulations. However, little is known about the ability of models to reliably represent the microphysical processes governing the precipitation. This study makes use of recent ground-based precipitation measurements at Dumont d'Urville station in Adélie Land to evaluate the representation of the precipitation microphysics in the Polar version of the Weather Research Forecast (Polar WRF) atmospheric model. During two summertime snowfall events, high-resolution simulations are compared to measurements from an X-band polarimetric radar and from a Multi-Angle Snowflake Camera (MASC). A radar simulator and a "MASC" simulator in Polar WRF make it possible to compare similar observed and simulated variables. Radiosoundings and surface-meteorological observations were used to assess the representation of the regional dynamics in the model. Five different microphysical parameterizations are tested. The simulated temperature, wind, and humidity fields are in good agreement with the observations. However, the amount of simulated surface precipitation shows large discrepancies with respect to observations, and it strongly differs between the simulations themselves, evidencing the critical role of the microphysics. The inspection of vertical profiles of reflectivity and mixing ratios revealed that the representation of the sublimation process by the low-level dry katabatic winds strongly influences the actual amount of precipitation at the ground surface. By comparing the simulated radar signal as well as MASC and model particle size distributions, it is also possible to identify the microphysical processes involved and to pinpoint shortcomings within the tested parameterizations.

1. Introduction

Precipitation is the major source term of the Antarctic surface mass balance and therefore the main input of water for the ice sheet. While the snow accumulation can be directly retrieved from networks of glaciological stakes (e.g., Favier et al., 2013) and ice cores (Thomas et al., 2017), the amount of precipitation that actually falls on the Antarctic surface still remains an open question. Significant progress has recently been made thanks to the deployment of ground-based radars (Gorodetskaya et al., 2015; Grazioli et al., 2017) and to the use of the CloudSat cloud-profiling radar (Behrangi et al., 2016; Lemonnier et al., 2019; Palerme et al., 2014). However, current ground-based precipitation radar measurements are limited to a few locations. In addition, the CloudSat product—albeit outperfoming ERA-Interim reanalyses in terms of snowfall climatology (Souverijns et al., 2018)—is contaminated by ground clutter in the first 1,200 m above the surface and misses a significant number of snowfall events due to the several-day revisit time of the satellite over most of the ice sheet.

Given the sparcity of precipitation measurements over Antarctica, the current assessment of the Antarctic precipitation and surface mass balance (The IMBIE team, 2018) still relies on reanalysis products (Wang et al., 2016) or Regional Climate Model (RCM) simulations (Agosta et al., 2019; van Wessem et al., 2018) that are mainly evaluated using surface mass balance observations. Reanalyses and RCM simulations often serve as references for evaluating the performances of General Circulation Models (GCMs), among which those involved in the fifth Coupled Model Intercomparison Project (Lenaerts et al., 2016; Previdi & Polvani, 2016; Palerme et al., 2017). Reanalyses, RCMs, and GCMs are also powerful tools to carry out climatological studies to assess the response of the Antarctic precipitation to the atmospheric circulation patterns (Genthon et al., 2003; Marshall et al., 2017; Monaghan et al., 2008), to the ozone depletion (Lenaerts et al., 2018), or to climate change (Palerme et al., 2017). Regarding the model performances, it

has been shown that the simulated Antarctic precipitation field strongly depends on the horizontal resolution (Genthon et al., 2009) and on the sea surface boundary conditions (Kittel et al., 2018; Krinner et al., 2014). Beyond these aspects, the modeled precipitation field is also expected to depend upon the subgrid parameterization of cloud and precipitation, which is paramount to the representation of precipitation formation as well as to the simulation of the low-level sublimation of snowfall in the katabatic layer over Antarctic coastal regions (Agosta et al., 2019; Grazioli et al., 2017). As subgrid cloud and precipitation parameterizations—and among them microphysical parameterizations including a detailed treatment of microphysical processes—have most of the time been developed for tropical and midlatitude conditions, the underlying physical assumptions and the arbitrary tuning of parameters (Tapiador et al., 2019) may not be adapted for polar regions.

To our knowledge, little attention, if any, has been paid to the ability of atmospheric models to represent the microphysical processes governing the Antarctic precipitation. This may be mostly explained by the lack of appropriate atmospheric measurements to constrain the representation of the solid-phase processes in models (Tapiador et al., 2018), and particularly over remote regions like Antarctica. Besides surface mass balance issues, the representation of microphysical processes over the ice sheets is also critical for simulating the surface energy budget (King et al., 2015; Li et al., 2017; Vignon et al., 2018) and the water isotopic composition of the snow surface as well as for for interpreting the isotopic signatures in ice cores (Gedzelman & Arnold, 1994).

Ground-based radar products are valuable data for evaluating and validating the representation of microphysical processes in atmospheric models (e.g., Gerber et al., 2018, Min et al., 2015, Nicholls et al., 2017). In the austral summer 2015–2016, the intensive Antarctic Precipitation, Remote Sensing from Surface and Space (APRES3) campaign of precipitation observation—including the deployment of a polarimetric radar and of a Multi-Angle Snowflake Camera (hereafter MASC)—took place at Dumont d'Urville (DDU) station, Adélie Land, East Antarctica. In particular, two major summertime snowfall events were intensively sampled and characterized by all the instruments. This campaign and especially these two snowfall events are an excellent opportunity to make use of ground-based observation to evaluate the simulation of Antarctic precipitation. In the present study, we use this unique data set to assess the ability of the Polar version of the Weather Research Forecast (Polar WRF) limited-area atmospheric model (Bromwich et al., 2013) to simulate the microphysics of precipitation in Adélie Land. The Polar WRF model, specifically adapted for polar studies, can be run with many options of subgrid microphysical parameterization. However, it is still not clear which one is the most suitable in terms of physics representation to be used—after a tuning phase—in climate simulations or weather forecasts in Antarctica. The objectives of the present study are to (i) reveal the key microphysical processes involved during Antarctic precipitation events in Adélie Land from radar and MASC measurements and to assess their representation in Polar WRF; (ii) investigate the sensitivity of the amount and structure of precipitation to the choice among state-of-the-art microphysical schemes; (iii) give recommendations for future evaluation and development of microphysical parameterizations to improve the simulation of precipitation over Antarctica.

The paper is structured as follows: Section 2 introduces the model, the observational data, and the evaluation methodology. Section 3 introduces the two study cases. Section 4 presents the results of the evaluation. Section 5 discusses the parameterization of key processes within the tested microphysical schemes. Section 6 draws the conclusions of the study.

2. Data and Methods

2.1. Observational Data Set From DDU Station

2.1.1. Standard Meteorological Observations

DDU station is located on the Petrels island at about 5 km north of the edge of the Astrolabe glacier, Adélie Land (−66.66° S, 140.00° E, 41 m a.s.l., Local Time = UTC + 10 hr). Standard measurements of meteorological variables (2-m temperature and humidity, 10-m wind, and surface pressure) are collected all year long at a 1-min temporal resolution. One radiosounding (Modem M2K2-DC type) is performed every day at 00 UTC. Wind profile data have been processed following the method presented in Vignon et al. (2019). Since November 2015, a wind-shielded weighing precipitation gauge (Pluvio2, manufactured by OTT) has been deployed, providing liquid water equivalent of precipitation at a 1-min temporal resolution. To remove the occurrence of "phantom accumulation," Pluvio2 data have been processed as in Grazioli et al. (2017).

2.1.2. MRR Data and Quantitative Precipitation Estimation

A Micro Rain Radar (MRR) was installed in November 2015 under a radome and provides since then vertical profiles of K-band (24 GHz) reflectivity and Doppler velocity over the first 3,000 m a.g.l. with a resolution of 100 m. Data were processed following the processing chain for snow hydrometeors developed by Maahn and Kollias (2012). The attenuation due to the radome was estimated and corrected for, following the method presented in Grazioli et al. (2017). To supplement the Pluvio2 measurements, precipitation rate has been estimated using a local reflectivity (at an altitude of 300 m a.g.l. corresponding to the first valid range gate)—snowfall rate relationship derived in Grazioli et al. (2017).

2.1.3. MXPol Radar, Hydrometeor Types, and Mixtures

A scanning X-band (9.41 GHz) dual-polarization radar (hereafter MXPol) was deployed in December 2015 and January 2016. It collected data at 75-m radial resolution with a maximum range of 30 km. It performed plan position indicator (PPI) scans, range height indicator (RHI) scans at 203° and 273°, and vertical profiles of the atmospheric column every 5 min. Details of the measurement system are given in Schneebeli et al. (2013) and Grazioli et al. (2017). Note also that from polarimetric variables, it is possible to classify the scattering hydrometeors into distinct classes following the semisupervised statistical clustering method developed by Besic et al. (2016). Furthermore, the application of the demixing method from Besic et al. (2018) makes it possible to infer the proportions of the different hydrometeor types in a given radar sampling volume.

2.1.4. MASC Data and Estimation of the Snow Size Distribution

The MASC is a ground-based instrument that automatically takes high-resolution and stereoscopic photographs of hydrometeors in free fall while measuring their fall velocity. The MASC uses three identical 2,448 × 2,048 pixel cameras that are triggered when a falling particle crosses two vertically separated lines of infrared detectors. Details on the MASC measurement system and deployment at DDU can be found in Garrett et al. (2012), Praz et al. (2017) and Grazioli et al. (2017). Praz et al. (2017) use a regularized multinomial logistic regression model to classify individual hydrometeors into six classes: small particle (SP), columnar crystal (CC), aggregate (AG), graupel (GR), planar crystal (PC), and combination of columnar and planar crystal (CPC). It also provides the degree of riming $\mathcal{R}_c$ and the melting probability MS (two continuous indices ranging between 0 and 1). During the feature extraction phase, the algorithm provides key characteristics of the snowflake like its maximum dimension (diameter of the circumscribed circle), its aspect ratio, and its orientation (from an ellipse fitting of the snowflake). Note that as the estimation of $\mathcal{R}_c$ and MS mostly rely on textural features, ill-defined small particles have been excluded in the calculation of these indices. Huang et al. (2017) developed an algorithm to retrieve particle size distributions (PSD) from MASC data. The authors highlight the good agreement between MASC-derived PSDs with those retrieved with a 2D Video Disdrometer (2DVD). Their study overall highlights the ability of the MASC to provide reliable information about the size distribution of snow particles. It is worth noting that the pixel resolution of the MASC is 33 μm limiting the characterization of snowflake properties if the typical size of the snow particle is smaller than 4–5 pixels ≈150 μm.

Note that standard volume PSD—estimated over a few minutes interval—require a sufficient number of particles to be reliable. However, owing to its relatively small sampling area ($S = 8.3\text{cm}^2$), this condition is often not achieved during the two studied events. Herein, we circumvent this issue by working with the quantity n_D (in mm^{-1}) that is the total number of snowflakes falling through the MASC during a period Δt (several days) and per diameter bin. Note also that in the present paper, we use the maximum snowflake dimension (from the three single views) to compute PSDs since the tested model microphysical schemes assume that a free-falling particle tends to fall in its maximum dimension.

Furthermore, Grazioli et al. (2017) reported that MASC measurements at DDU are contaminated by blowing snow. To solve this issue, Schaer et al. (2018) used a Gaussian mixture model to discriminate between precipitation and blowing snow images in MASC data. As Polar WRF does not account for blowing snow in its current set of parameterizations, removing blowing snow from MASC data makes it possible to directly compare precipitation PSDs between the model and the MASC.

2.2. Polar WRF Simulations

2.2.1. Model Description and Simulation Design

This work is based on Version 3.9.1 of Polar WRF. It contains an optimized physical package adapted for polar regions with a particularly enhanced representation of the sea ice and of the heat transfer through the snow pack (Bromwich et al., 2013; Hines et al., 2015). As a "final" product of the modeling,

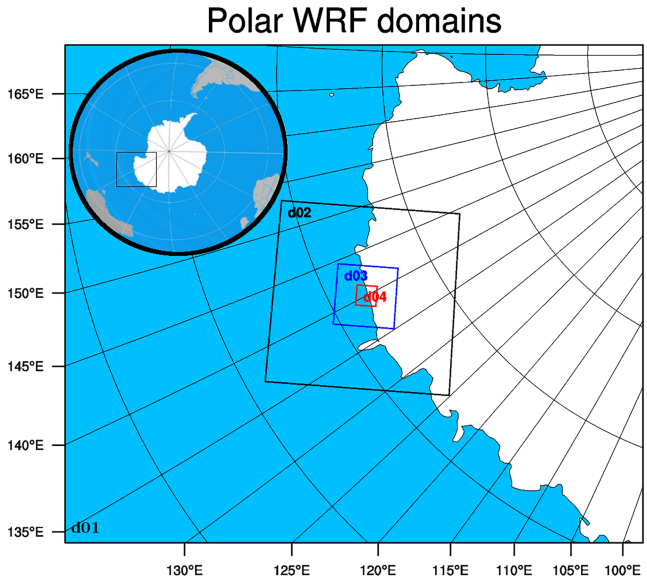

Figure 1. Polar WRF simulation domains. Domains d01, d02, d03, and d04 have an horizontal resolution of 27, 9, 3, and 1 km, respectively.

Tapiador et al. (2018) stress that precipitation suffers from the multiplicative effect of errors in both thermodynamical and dynamical processes. Herein, as we mostly aim to focus on precipitation and the related microphysics, we should ensure a correct regional atmospheric dynamics and proper baseline meteorological variables. This particularly implies to run high-resolution simulations. We have thus set the following modeling framework up.

The model has been run with a downscaling method where a 27-km resolution parent domain contains a 9-km resolution nest, which contains a 3-km resolution domain, which itself contains a 102 × 102km nest at a 1-km resolution (see Figure 1). All domains have been built with the same polar stereographic projection, and they are all centered over DDU. The nesting is one way; that is, no information is passed in return from one domain to its parent. Lateral forcings, sea ice concentration, sea surface temperature, and initial conditions are from the European Center for Medium Range Forecast ERA5 reanalysis, which has a 0.25 × 0.25° horizontal resolution. This reanalysis product shows significant improvement in terms of vertical temperature, humidity, and wind profiles in the DDU region compared to the previous ERA-Interim reanalysis (Vignon et al., 2019), which itself was shown to have the best large scale circulation patterns over Antarctica among five reanalysis products (Bracegirdle & Marshall, 2012). As recommended by Deb et al. (2016), the Bedmap2 1-km resolution Antarctic topography from Fretwell (2013) has been used. The model is run with 66 vertical levels among which 23 are located in the first 3,000 m above the ground surface. As more thoroughly developed in section 3, the model evaluation will be conducted on two precipitation events. Simulation of the first event starts on 27 December 2015 00 UTC and simulation of the second event starts on 26 January 2016 00 UTC, that is, 24 hr before the analysis starting time (see section 4). To allow for a concomittant comparison between in situ observations and simulations and to ensure a realistic synoptic dynamics in the model, the 27, 9, and 3-km resolution domains have been nudged above the boundary layer toward ERA5 reanalysis (for zonal and meridional wind speed, temperature, and specific humidity) with a relaxation time scale of 3, 6, and 9 hr, respectively. This analysis nudging only helps in providing the best lateral forcings for the free 1-km resolution domain, which will be the sole domain analyzed hereafter. The physics options employed throughout the paper include the new version of the Rapid Radiative Transfer Model for GCMs radiation scheme for longwave and shortwave spectra, the Noah land surface model with adaptations by Hines and Bromwich (2008), and the Mellor-Yamada-Nakanishi-Niino (MYNN) planetary boundary layer scheme coupled with its associated surface layer scheme. For domains with a resolution greater or equal than 9 km, the Kain-Fritsch cumulus scheme has been activated. This physical package was set after consideration of previous evaluation studies (Bromwich et al., 2013; Deb et al., 2016; Listowski & Lachlan-Cope, 2017; Young et al., 2019) and preliminary sensitivity tests over Adélie Land.

2.2.2. Microphysical Parameterizations

Polar WRF has an extensive set of microphysics options, including bin models—which predicts the evolution of hydrometeor numbers in size bins allowing for a complete description of the particles distribution—and single- and double-moment bulk parameterizations that predict mass and mass + number concentrations of hydrometeor species, respectively. Bin models are too computationally expensive for being used for operational purposes or for long-range climate studies. As our study will focus on regional simulations, we will perform sensitivity tests upon the choice among bulk schemes only. Using recent airborne measurements, Listowski and Lachlan-Cope (2017) have assessed the performances of five bulk microphysical schemes in Polar WRF to represent clouds over the Antarctic Peninsula. The authors showed that the WRF single-moment scheme 5—WSM5 (Hong et al., 2004), used in the Antarctic Mesoscale Prediction System—and the WRF Double moment scheme 6—WDM6 (Lim & Hong, 2010), an upgrade version of WSM5—showed the largest biases in observed supercooled liquid water. On the other hand, the double-moment Morrison scheme (Morrison et al., 2005, 2009), Thompson scheme (Thompson et al., 2008), and Milbrandt scheme (Milbrandt & Yau, 2005) show better prediction of occurrences of clouds and cloud phase. Grazioli et al. (2017) report a significant part of rimed snowflakes at DDU station suggesting the frequent occurrence of supercooled liquid water above the station. The presence of supercooled liquid water over Adélie Land—especially in summer—has been confirmed by in situ lidar measurements (Del Guasta et al., 1993) and by the DARDAR (raDAR-liDAR) satellite product (Listowski et al., 2019). In this study we will therefore focus our analysis on simulations performed with the Morrison, the Thompson, and the Milbrandt schemes. A simulation with WDM6 has also been carried out to assess to what extent the conclusions of Listowski and Lachlan-Cope (2017) about cloud properties over the Antarctic Peninsula can be extended to precipitation over Adélie Land. Moreover, we will also consider simulations using the advanced predicted particle properties (P3) bulk scheme (Morrison & Milbrandt, 2015). Along with the Morrison and the Thompson scheme, the P3 scheme has also shown considerable improvement in the simulation of the cloud fraction, liquid hydrometeors, and cloud radiative effect in West Antarctica compared to the standard WSM5 scheme (Hines et al., 2019).

To help the simulation comparison, we provide in the following paragraphs a few elements of information about the five tested microphysical schemes. Further details regarding the primary and secondary ice generation are given in Listowski and Lachlan-Cope (2017) and Young et al. (2019). Note that the performances of each scheme strongly depend upon the specific tuning of numerous parameters (Tapiador et al., 2019). In this paper, we use the standard—but physically consistent and robust—configurations of the microphysical schemes, and we will see that our evaluation will pinpoint processes that should be revisited—or that deserve further tuning—for future applications in this particular region of the globe. A summary of the empirical values and of the formulations of microphysical processes in the WRF microphysical schemes is presented in Tapiador et al. (2019).

Morrison scheme: The Morrison scheme (Morrison et al., 2005, 2009) is a single-moment scheme for cloud droplets. The default value of the droplet number concentration in WRF (250 cm^{-3}, typical for mid-latitude conditions) has been set to a more appropriate value for polar applications in Polar WRF (50 cm^{-3}, see Hines & Bromwich, 2017, and Hines et al., 2019). Cloud ice and snow are delineated with a diameter threshold of 125 μm. Rain, cloud ice, snow, and graupel classes are treated with a full double-moment approach. All particles are assumed spherical, and each class has a fixed constant density. All categories but cloud droplets are parameterized with an inverse-exponential size distribution.

Milbrandt scheme: The Milbrandt scheme (Milbrandt & Yau, 2005) uses a full double-moment treatment for the six hydrometeor species: cloud droplets, cloud ice, rain, snow, graupel, and hail. All species are represented by a generalized Gamma size-distribution function that reduces to an inverse-exponential for ice, snow, and graupel types. All categories are assumed to be spherical with a constant bulk density except snow whose density varies inversely with size. The autoconversion of cloud ice to snow is parameterized by converting the part of the size distribution of cloud ice whose diameter is greater than 250 μm. The number of cloud condensation nuclei (CCN) is calculated following the hyperbolic functions of Cohard and Pinty (2000).

Thompson scheme: The Thompson scheme (Thompson et al., 2008) is a single-moment scheme for cloud droplets, graupel, and snow species and a double-moment scheme for cloud ice and rain drops. Cloud droplet concentration is fixed to 100cm^{-3}. Akin to the Morrison and Milbrandt schemes, cloud droplets,

cloud ice, and rain particles are assumed to be spherical, and their respective distributions follow a generalized Gamma law. Graupel particles are also assumed spherical and the respective distribution obeys a generalized Gamma law for which the intercept parameter depends on the mixing ratio. A specific treatment is applied for snow hydrometeors. The latter are assumed to have a nonspherical shape with a bulk density that varies inversely with diameter (in agreement with many observational studies, see Thompson et al., 2008). In addition the snow size distribution is a combination of a gamma function and an exponential function that accounts for the "super-exponential" number of very small particles. The intercept parameter depends upon the snow water content and air temperature. In the Thompson scheme, snow forms by vapor deposition onto cloud ice until crystal size exceeds 200 μm. Note that an advanced "aerosol-aware" version of the Thompson scheme (Thompson & Eidhammer, 2014) is available in Polar WRF. In the present study we use the original Thompson scheme mostly because the aerosol-aware option is not directly compatible with the current version of the WRF radar simulator that is used hereafter (see next subsection). Moreover, a detailed study of the aerosols-clouds interactions over Antarctica is beyond the scope of the present study.

WDM6 scheme: The WDM6 scheme (Lim & Hong, 2010) uses a double-moment approach for cloud droplets and rain drops and a single-moment approach for ice, snow, and graupel particles. The cloud droplet and rain size distributions are parameterized with generalized gamma functions whose slope and intercept parameters depend on mass and number mixing ratios. The cloud ice number concentration is diagnosed as a function of the ice mass mixing ratio. Snow and graupel particles have a fixed density, and they are assumed to be spherical and to have size distributions following an inverse-exponential function. The intercept parameter for the snow size distribution decreases with increasing temperature to represent the broadening of the snow spectra at higher temperature.

P3 scheme: The P3 parameterization moves away from the paradigm of separating ice into different species with fixed characteristics. It instead allows the ice particle properties to continuously vary with time (Morrison & Milbrandt, 2015). In the liquid phase, cloud droplets are treated with a single-moment approach while both mass and number mixing ratios of rain are prognostically calculated. Cloud droplets and rain drops are assumed to follow a Gamma distribution. In the unique solid phase, the scheme prognoses the ice mass mixing ratio, the ice number concentration, the rime mass and the rime volume. Ice particles are assumed to obey to a Gamma size distribution. As mentioned in Morrison and Milbrandt (2015), the intercept parameters of the Gamma function becomes greater than 0—and the distribution differs from an inverse exponential—only when the mean particle size is lower than ≈0.17 mm. The mass-diameter relationship and the velocity diameter one depend on the size of the ice hydrometeors as well as on the rime mass fraction and rime density. Even though an advanced version of the P3 scheme has been made available in the fourth version of WRF (Milbrandt & Morrison, 2016), we use here the original version of the scheme because it is the only one available in Polar WRF v3.9.1 and compatible with the current version of the radar simulator.

2.3. Model Evaluation Strategy and Methodology

As the standard outputs from Polar WRF using bulk microphysical parameterizations (number and mass mixing ratios) differ from MASC and X-band radar quantities, an evaluation methodology has to be developed in order to use radar and MASC information to evaluate the representation of the microphysical processes in the model. This necessarily implies a postprocessing of model variables. Hence, we will use a radar and a MASC simulator that convert, under some assumptions, Polar WRF output variables to radar and MASC quantities that can then be directly compared with observational variables.

2.3.1. From Polar WRF Outputs to Radar Variables: The CR-SIM Forward Radar Simulator

The Cloud Resolving Model Radar SIMulator (CR-SIM) uses output variables from WRF simulations to provide idealized model scanning radar observations. We use here Version 3.1, which handles the Morrison, Thompson, Milbrandt, and P3 microphysical scheme (not available for WDM6). CR-SIM uses the T-matrix method for computing the scattering properties of cloud water, cloud ice, rain, snow, graupel, and hail hydrometeors. It is able to account for different radar frequencies among which a frequency close to the one of MXPol (9.5 GHz). All particles are modeled as dielectrically dry spheroids. Subsequently ice, snow, graupel, unrimed ice, partially rimed ice, and hail are represented as mixture of air and dry solid ice. The complex scattering amplitudes are precomputed and stored as lookup tables for equally spaced particle sizes using the Mishchenko's T matrix code for nonspherical particles at a fixed orientation and for elevation angles from 0 to 90°. Details about CR-SIM can be found in the documentation (radarscience.weebly.com). In this

study, CR-SIM has been configured as a virtual MXPol radar at DDU, that is, with the same geographical location and altitude, the same frequency, the same beamwidth and range, and the same sensitivity. For each hydrometeor type, we have used the recommended (default) lookup tables as summarized in Table S1 of the supporting information. Thanks to MASC measurements, it is possible to validate some of the assumptions for the properties of precipitating hydrometeor types (snow, rain, graupel, unrimed, and partially rimed ice). This aspect is presented in section S1. It is worth mentioning that the analysis of the CR-SIM outputs and a comparison with MXPol data revealed that the polarimetric quantities in the snow and ice phase are not properly reproduced—even the correct ranges of values—by the present T matrix-based radar simulator (at least over the two precipitation cases studied hereafter; see Figure S2). Therefore, we will restrict the comparison between observed and simulated radar data to the reflectivity and Doppler velocity.

2.3.2. From Polar WRF Outputs to Surface PSD: A MASC Simulator

For an appropriate comparison between precipitation PSDs estimated from MASC data and those in Polar WRF simulation—which vary at each time step depending on atmospheric conditions and total number concentration and mixing ratio—we have developed a so-called "MASC simulator" for the model. The detailed description and derivation of this simulator is presented in Appendix A. Thanks to this simulator, it is possible to directly compare the PSD (quantity n_D) between MASC measurements and the model. Note that we use a 0.05-mm bin size for calculating PSDs in both MASC and model.

3. Description of the Two Precipitation Events

During the APRES3 campaign, two major precipitation events were successfully sampled by the whole set of instruments. These two precipitation events will serve as two evaluation cases for Polar WRF. Maps of the synoptic conditions during the two events are given in Figure S3.

The first event (hereafter Event 1) occurred between 28 and 31 December 2015. A synoptic weather system arrives to the west of DDU. On 29 December at 00 UTC, a warm front associated to the system is passing above DDU station. The X-band radar starts to see reflectivity signal at $z = 3{,}000$ m on 28 December at 03 UTC (Figure 2a). Despite significant reflectivity values in the first 3,000 m until the end of the 30 December (regardless the lull during the afternoon of the 30 December), the precipitation rate at the surface (Figure 2b) is relatively weak and peaks at 1.5 mm/hr in the early morning of the 30 December. A mismatch between reflectivity and surface precipitation amount is particularly noticeable during the afternoons of the 28 and 29 December. This is actually a signature of the low-level sublimation of precipitation by the relatively dry katabatic winds blowing from the interior of the Antarctic Plateau, as evidenced in Grazioli et al. (2017) and Durán-Alarcón et al. (2019). During the first part of the precipitation event, the low-level wind speed increases up to 28 m/s but the direction remains easterly (Figures 2i and 2j). This reflects the strengthening of the katabatic flow due to the increase of the large-scale pressure gradient during the approach of the synoptic weather system. In addition, while the atmospheric column above DDU is saturated with respect to ice above 1,000 m due to clouds and precipitation, the relative humidity strongly decreases with decreasing height down to the surface (Figures 2b and 2h). This leads to a partial or total sublimation of the snowflakes before they reach the ground surface. From the 30 December at 06 UTC, the synoptic system slightly protrudes over the Antarctic continent and decays. As a consequence, the near-surface wind dramatically weakens and becomes northwesterly. In the afternoon of 30 December, the center of the weakened cyclone has passed east of DDU and advects moisture from the east at its southern flank, explaining the last peaks of snowfall in the time series. Figures 2e and 2f show that snow precipitation during Event 1 mostly consists in small particles (55.4%), aggregates, and graupel (approximately 17% each). The near-surface temperature gently swings around 0 ° C. The melting probability estimated from MASC-sampled snowflakes is most of the time close to zero, but a few rain droplets have been photographed during the event (not shown).

The second event (hereafter Event 2) occurred between 27 and 29 January 2016. A synoptic cyclone stands to the west of DDU, and it advects moisture at its eastern flank leading to a band of precipitation reaching Adélie Land. The cyclone progressively weakens and dissipates still at the west of DDU until the 30 January. At DDU station, significant reflectivity values are detected by MXPol from the 27 January at 05 UTC until the 29 January at 08 UTC. Reflectivity values and precipitation rates reach higher values than during Event 1 (Figures 3a and 3b). The near surface wind speed increases—peaking in the morning of 28 January—as the cyclone approaches DDU, but its direction remains easterly up to a height of 1,000–1,500 m (Figures 3d, 3i, and 3j). The strong shear in wind direction and the slight temperature inversion at $z \approx 1{,}500$ m (Figures 3g and 3j) indicate the clear transition between the remnant of katabatic layer flowing easterly and the warm

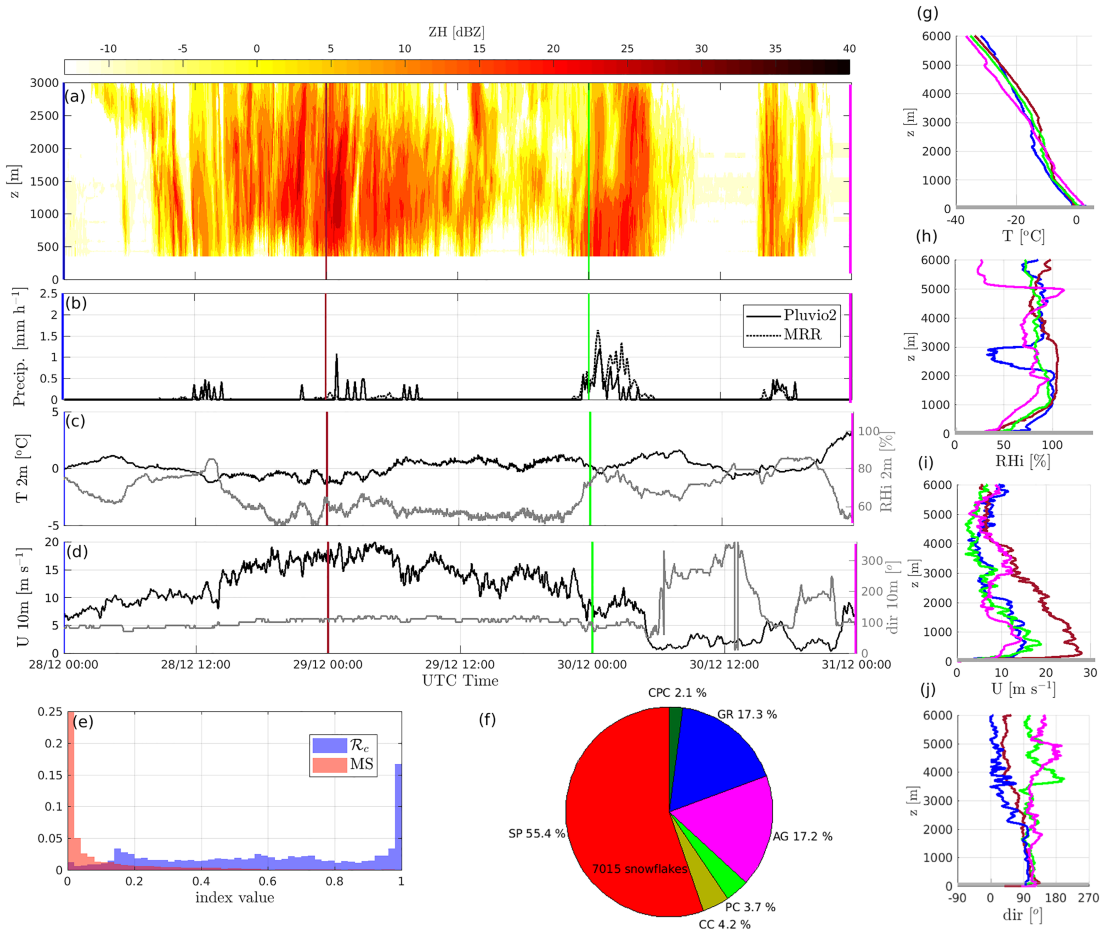

Figure 2. Depiction of the first precipitation event from in situ data at DDU station. (a) Time-height plot of the X-band reflectivity measured by MXPol. (b) Time series of the precipitation rate from Pluvio2 (solid line) and MRR (dotted line) data. (c, resp. d) Time series of the 2-m temperature (resp. 10-m wind speed) in black line and relative humidity with respect to ice (resp. 10-m wind direction) in gray line. (e) Histogram of the Riming index $\mathcal{R}_c$ (blue) and Melting probability MS (red) of snowflakes sampled by the MASC during the period corresponding to panels a–d. Note that small particles are not included in this statistics since texture indices like $\mathcal{R}_c$ and MS are reliable only for sharp snowflakes and crystals. (f) Relative proportions of hydrometeor types identified from MASC data. (g–j) Vertical profiles of temperature, relative humidity with respect to ice, wind speed, and wind directions, respectively, in radiosonde data. Colors refer to the vertical lines in panels a–d indicating the radiosounding times.

and moist air mass advected above from the north. The near-surface air remains unsaturated even during the snowfall peaks (Figures 3b and 3h), suggesting that the low-level sublimation still occurs during this event. This is confirmed by the inspection of individual vertical profiles of radar reflectivity but the relative importance of low-level sublimation is much less than during Event 1. Figure 3e shows that the melting probability of the snowflakes is weak in agreement with the negative 2-m temperatures (Figure 3b). The snowflakes sampled by the MASC have been mostly classified as small particles (Figure 3f), but the aggregate (15.3%) and graupel (9.3%) proportions are also significant.

The total accumulated precipitation during Event 1 (resp. Event 2) is 3.4 mm (resp. 13.0 mm) from Pluvio2 data and 4.9 mm (resp. 15.3 mm) from MRR estimations. Albeit weak, the precipitation amount during these two events is significant for DDU, given that the 1995–2015 yearly averaged (resp. December–January averaged) accumulated precipitation from ERA-Interim reanalyses is 543.1 mm (resp. 104.3 mm) and that the estimated yearly (resp. December–January) accumulation from MRR data is comprised between 739.5 (resp. 41.3) and 989 mm (resp. 59.3 mm). Moreover, it is worth mentioning that more than 65% of the yearly amount of precipitation at DDU is explained by snowfall events whose intensity ranges between 0 and 2 mm/hr (Grazioli et al., 2017). Even though we cannot state that the two precipitation cases studied here are statistically representative in terms of synoptic and regional dynamics, their intensities are nonetheless typical of most events affecting the coastal Adélie Land.

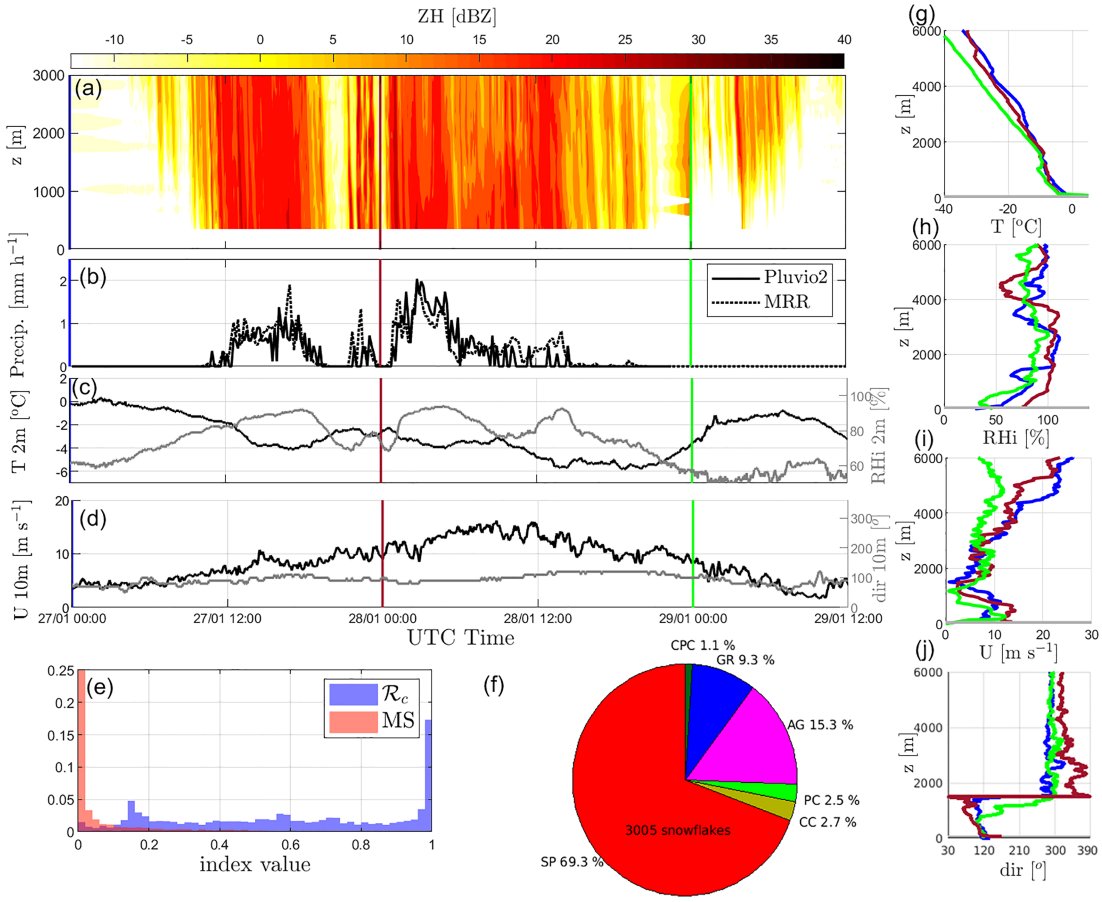

Figure 3. Same as Figure 2 but for the second precipitation event.

4. Results of the Model Evaluation

This section presents the results of the Polar WRF evaluation during the two precipitation events at DDU. To ensure that the observation-simulation differences can be primarily attributed to the microphysical scheme, we have verified that the regional atmospheric dynamics around DDU is well captured—and the baseline meteorological variables well represented—by Polar WRF and consistent between the different simulations (see details in Appendix B).

4.1. Event 1

4.1.1. Surface Precipitation

Figure 4a compares the time series of accumulated precipitation at DDU from MRR and Pluvio2 data and from five Polar WRF simulations with the five different microphysical schemes during Event 1. One can first notice the higher accumulated precipitation estimated from MRR data (4.9 mm) than measured with the Pluvio2 (3.4 mm) at the end of the event. Such difference may be explained by uncertainties in the reflectivity-precipitation relation as well as by the low-level sublimation process that occurs during this event (see previous section) and that can remove a significant part of the precipitation between 300 m a.g.l.—height at which the reflectivity-precipitation relation has been derived—and the ground surface. Note also that during infrequent periods of high precipitation intensity—like around 00 UTC 30 December 2015—the MRR precipitation rates are subject to higher uncertainties because the reflectivity—snowfall rate relationship is applied in a low-confidence range (see Figures 9 and 12 in Grazioli et al., 2017).

Thompson, WDM6, and P3 microphysical schemes give a poor total accumulated precipitation, with simulated values lower than 1 mm, that is, more than three times less than the measurements. These very low values are not confined to the DDU grid point, but they extend along a “dry tongue” that follows the Terre Adélie coast (Figure S5). Simulations with the Morrison and Milbrandt schemes give more satisfactory values, close to 2.2 mm. In all simulations, the difference with observations at DDU is mostly explained by the

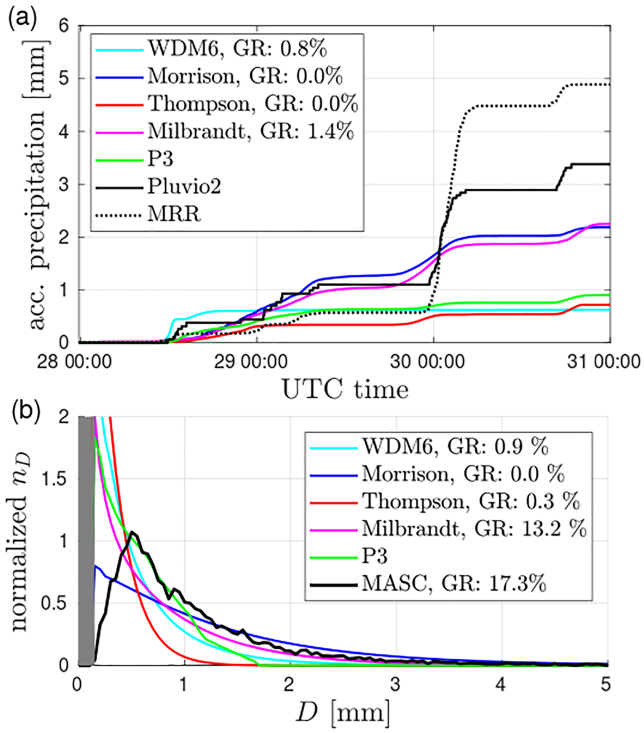

Figure 4. (a) Time series of the accumulated precipitation at DDU station during Event 1 (December 2015) from MRR data (dotted black line), from Pluvio2 data (solid black line), and Polar WRF simulations with five different microphysical schemes (colored lines). Numbers in the legend indicate the percentage of graupel in the accumulated precipitation for simulations with a "graupel" class. (b) PSD during Event 1 from MASC data (black line) and from Polar WRF simulation outputs using the MASC simulator (colored line). The quantity, which is plotted in y axis, is n_D (see sections 2.1.4 and 2.3.2) calculated over the whole Event 1 period, summed over snow and graupel types (except P3 for which the unique ice type is shown) and normalized by the integral value over the full diameter range. The first three bins ([0–0.15 mm] range) have been shaded because they include the uncertainty range of MASC data. Numbers in the legend indicate the percentage of graupel particles.

underestimation of the precipitation peak on 30 December between 00 and 03 UTC. Note also that despite major regional or local differences like those at DDU, the accumulated precipitation show less discrepancies between the different simulations when looking at the domain-averaged values (Figure S4a). This is consistent with the fact that the domain integrated precipitation primarily depends on the moisture convergence, the latter being driven by the advection at the domain boundaries that is relatively similar between the simulations owing to the nudging of the external nests.

In terms of precipitation type, the surface precipitation during Event 1 in the WDM6, Morrison, and Thompson simulations is mostly composed of snow. In the Milbrandt simulation 0.03 mm (≈1.4 %) falls as graupel. In the P3 simulation, 1.8% of the precipitation mass at the surface corresponds to rime.

Regarding the size distribution of surface precipitation, Figure 4b compares the event-integrated size distributions of solid precipitation at the surface in the simulations with that retrieved from MASC measurements. We focus here on solid particles in free fall (that can be easily detected by the MASC), that is, graupel and snowfall particles. For the P3 scheme the PSD of the unique "ice" type is plotted. Note that PSDs have been normalized by the total number of particles. Interestingly, the n_D curve corresponding to MASC data has a clear mode around $D = 0.5$ mm. Unlike MASC observations, all simulations show a monotonically decreasing n_D. Indeed, the increase in n_D with increasing diameter for very small particles cannot be captured by an inverse-exponential function or a "super-exponential" function for the PSD of the "snow" hydrometeors as assumed in the tested microphysical schemes except P3. Simulations with the Thompson, WDM6, and P3 microphysical scheme have too many very small particles ($D < 0.5$ mm) at the surface. Moreover, the simulation with the Thompson scheme strongly underestimates the number of particles with $0.5 < D < 3$ mm. On the other hand, the size distribution from the simulation with the Milbrandt scheme agrees reasonably

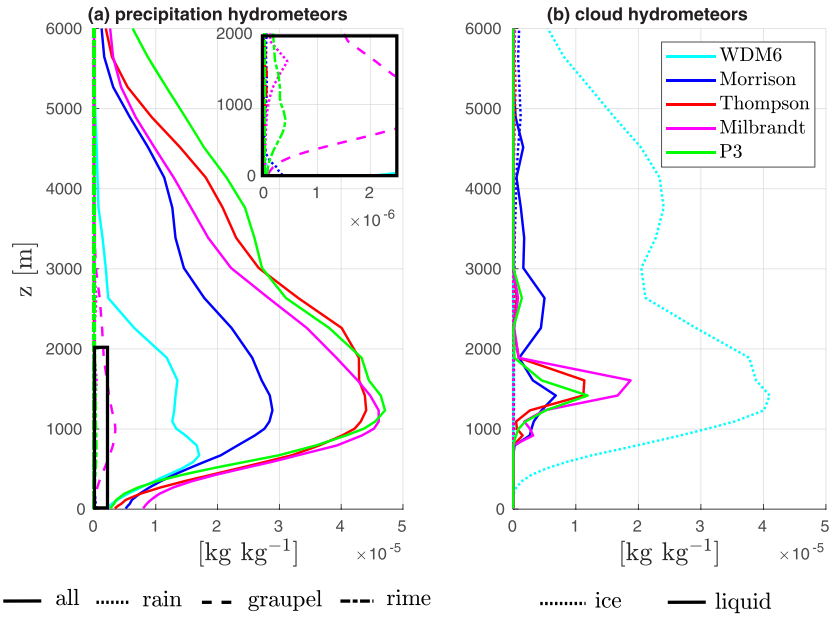

Figure 5. Averaged vertical profile of mass mixing ratios of precipitation hydrometeors (a) and of cloud condensates (b) above DDU in Polar WRF simulations during Event 1. In panel a, solid lines show the sum of snow, rain, and graupel types (except for the simulation with P3 microphysics—green line—for which the sum of the rain and the ice type is plotted), dotted lines show the rain type profiles and dashed lines show the graupel type profiles. For the P3 simulation, the mass of rime is plotted in dotted-dashed line. In panel b, dotted line show the cloud ice profiles and solid lines show the cloud liquid water profiles.

well with MASC observations for $D > 0.5$ mm. It can also be pointed out that only the Milbrandt simulations shows a significant percentage of graupel particles—in number—at the surface (13.2% vs. 17.3% for the MASC).

4.1.2. Hydrometeor Mass Mixing Ratios

Figure 5 shows the averaged vertical profiles of the mass mixing ratios of "precipitation" hydrometeors (snow, graupel, and rain; Figure 5a) and of "cloud" condensates (cloud ice and cloud droplets; Figure 5b) above DDU in Polar WRF simulations during Event 1. Note that for the simulation with the P3 microphysical scheme, the sum of the rain and ice types is plotted in solid line in Figure 5a. The first striking feature is the distribution between the cloud ice phase and the snow phase in WDM6 simulation. Unlike Morrison, Thompson and Milbrandt schemes in which the snow phase strongly dominates below $z = 6{,}000$ m, most of the condensed water mass is in the cloud ice phase above $z = 1{,}000$ m. Between $z = 1{,}000$ m and $z = 3{,}000$ m, the Thompson, Milbrandt, and P3 schemes give similar mass mixing ratios of precipitation hydrometeors with a peak at approximately 4.5×10^{-5} kg/kg slightly above $z = 1{,}000$ m. The shape of the profile in the Morrison simulation is similar but the averaged amount of precipitation does not exceed 3×10^{-5} kg/kg. In all simulations, the hydrometeor mass mixing ratio strongly decreases with decreasing height below 1,000 m evidencing the representation of the low-level sublimation process. Considering the sum of "sedimenting" condensates—cloud ice, graupel, rain, and snow (excluding the cloud droplets that are either assumed suspended or that have a very low sedimentation velocity)—the difference between the maximum value in the profile and the surface value is the highest in the WDM6 simulation while it is the lowest in the Morrison simulation. This result is not locally restricted to DDU because similar conclusions can be drawn when considering the domain-averaged vertical profiles (Figure S7). Overall, Figure 5 reveals the strong dependency of the amount of surface precipitation upon the representation of the snow and ice sublimation during Event 1. It also highlights that the relatively "best" accumulated precipitation in the Morrison and Milbrandt microphysics (Figure 4a) actually corresponds to two very different vertical profiles of precipitation mixing ratios.

Furthermore, Figure 5b shows that the Morrison, Thompson, P3, and Milbrandt schemes produce supercooled cloud liquid water. Above DDU, a particularly pronounced peak between 1,000 and 2,000 m is noticeable in P3, Thompson, and Milbrandt simulations but over the whole domain, and especially over

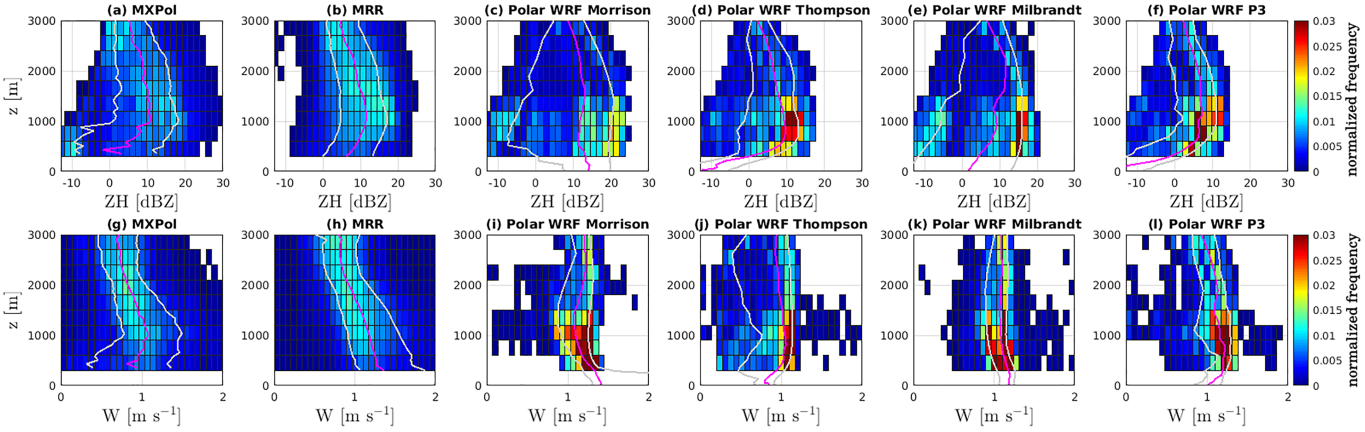

Figure 6. Joint probability distributions of the X-band reflectivity ZH (first row) and of the reflectivity-averaged vertical Doppler velocity W from MXPol data (a and g), from MRR data (b and h), and from Polar WRF simulations with four different microphysical schemes (c–f and i–l). Note that radar data are not available in the first 300 m. Hence, even in model simulations, the 0- to 300-m altitude range is not accounted for in the joint probability distribution calculation. Magenta lines are the median vertical profiles, and gray lines are the vertical profiles of the 20th and 80th percentiles. MRR K-band reflectivity has been converted to X-band reflectivity using the formula in Grazioli et al. (2017).

the ocean, the Morrison scheme shows the largest content of cloud liquid in particular between 2,000 and 3,000 m of altitude (see Figure S7). The absence of supercooled liquid water in the WDM6 scheme concurs with the results of Listowski and Lachlan-Cope (2017). In addition, only the Milbrandt scheme produces a significant quantity of graupel, which peaks at $z = 1{,}000$ m above DDU (Figure 5a). Apart from graupel, the Morrison scheme produces a small quantity of rain near the surface (see inset in Figure 5a) that corresponds to a very partial melting of snowflakes owing to the slightly positive near-surface temperatures.

4.1.3. Comparison to Radar: Vertical Profiles of Reflectivity and Doppler Velocity

A common way to compare simulations and radar observations are the contoured frequency by altitude diagram (CFAD, e.g., Yuter & Houze, 1995) of the reflectivity. Albeit very useful for statistical analyses, CFADs do not inform about the distribution of radar variables along the altitude axis. In Figure 6, we rather compare the 2-D joint distributions of the reflectivity (first row) and of the mean reflectivity-weighted Doppler velocity (second row) above DDU station from the two radars and from four Polar WRF simulations. Medians and two additional quantiles are shown in solid lines. Even though the vertical statistics are estimated above one location—to benefit from the vertically profiling MRR—we have also calculated the same vertical profiles in MXPol and in the simulations but integrating over the whole 203° RHI (perpendicular to the coastal edge). Fairly similar results and comparisons were obtained compared to the one-point profiles for the two events (not shown). At this stage, it is also worth remembering that the CR-SIM radar simulator cannot perform on simulations with the WDM6 microphysical scheme.

In terms of reflectivity, the first interesting point regarding the observations is the difference between MRR and MXPol distributions below $z = 1{,}000$ m. Indeed, MXPol shows more frequent low (less than −10 dBZ) reflectivity values. This can be explained by a higher sensitivity of the MXPol instrument compared to the MRR due to the attenuation of the radome shielding the MRR. Those low-reflectivity signals may correspond to low-level cloud particles or to light virgas. In both radars data, the median reflectivity peaks at $z \approx 1{,}000$ m and then decreases with decreasing height due to the low-level sublimation. A clear peak in the median reflectivity profile is noticeable in the simulations with the Thompson and P3 schemes. Such peak is not present (resp. only slightly distinguishable) in the Morrison simulation (resp. Milbrandt simulation) while a clear maximum in the mass mixing ratio profile was pointed out in Figure 5. This apparent paradox can be explained by the continuous increase in the hydrometeor size as snow falls in the Morrison and Milbrandt simulations. As the atmosphere is not saturated between the ground and 1,000 m, the growth mechanism should necessarily be aggregation. Further investigation indeed reveals that the event-averaged snow mean mass diameter monotonically increases from 0.432 mm (resp. 0.434 mm) at $z = 3{,}000$ m to 1.266 mm (resp. 1.360 mm) near the surface in Morrison (resp. Milbrandt) while this diameter decreases in the first 1,000 m above the surface in the other simulations. The increase in diameter size thus compensates for the decrease in hydrometeor mass and maintains the near-surface reflectivity—that roughly depends on the sixth moment of the size distribution (e.g., Straka, 2009, Chap. 2)—at relatively high values. This result is also

in agreement with the relatively higher proportion of large diameters in the surface PSD (Figure 4b) compared to the Thompson and P3 simulations. Note that in reality, the low-level sublimation process can lead to an increase in the mean mass diameter—owing to a preferential sublimation of small particles—and thus not reflect a growth of snowflakes. However, such an increase in mean mass diameter due to sublimation cannot be represented by the current parameterization of sublimation (see section 5).

Looking at the joint distributions, one can point out that above 2,000 m, the reflectivity is generally overestimated in the Morrison simulation while the median value, and the width of the distribution is underestimated in the P3 simulation. Below $z = 1{,}500$ m, the Milbrandt scheme and especially the Morrison scheme show (relatively) too frequent high (>10 dBZ) reflectivity values compared to observations. On the other hand, the P3 scheme, and to a lesser extent the Thompson scheme, underestimate the occurrence of reflectivity values >15 dBZ. During the peak of precipitation on 30 December at 00 UTC, the two radars show an intense reflectivity (≈20 dBZ) from 300 to 3,000 m of altitude while simulations with the Thompson and the P3 schemes show weaker reflectivity values with a strong decrease in the first 500 m above the surface. The underestimation of precipitation in the latter simulations evidenced in Figure 4 seems thus first explained by an excessive sublimation close to the surface during the precipitation peak (see also the time-height plot in Figure S9).

Regarding the Doppler velocity (panels g-l in Figure 6), one can notice the continuous increase with decreasing height of the median velocity below $z = 2{,}500$ m in MRR data, whereas the median velocity decreases below $z = 1{,}000$ m in MXPol data. This can be attributed to the higher sensitivity to smaller—and therefore slower—particles near the surface in MXPol. Except for the P3 simulation, the model does not reproduce the increase in median velocity with decreasing height. In addition, all simulations underestimate the spread of velocity values compared to radar data. We have checked that this result does not depend on the difference in time resolution between the different data sets. Provided that the dynamical vertical velocity is similar in all simulations, the differences in the Doppler velocity distributions between the simulations are therefore mostly due to the microphysical schemes. It should be specified that although the CR-SIM simulator makes use of the turbulent kinetic energy (TKE) to diagnose the velocity spectrum width, no information about turbulence is used in the calculation of the Doppler velocity. This may explain some differences in the velocity distribution between simulations and radar observations, especially in the first 1,500 m above the surface (turbulent katabatic layer) where the two 80–20 interquantile range gets wider only in the observations. Indeed, the sampling radar volumes in the observations are much smaller than the model mesh volume with a kilometer-scale base area. Hence, the mean dynamical vertical velocity in the model is by nature substantially different from that in a radar volume that depends on subkilometer (turbulent) eddies. To get an idea of how the inclusion of the turbulent velocity might affect the simulated Doppler velocity, one may estimate the order of magnitude of the turbulent vertical velocity in the model. In neutral conditions like within a well-mixed katabatic layer, the turbulent vertical velocity scale (square root of the variance of the vertical velocity) reads $(0.444\,\mathrm{TKE})^{1/2}$ in the second order MYNN planetary boundary layer scheme. During Event 1, the simulated TKE at $z \approx 1{,}000$ m is comprised between 0 and 1.1 m^2/s^2; that is, the turbulent vertical velocity is ≈0–0.70 m/s. This interval broadly covers the Doppler velocity range in the observational data, suggesting that small-scale turbulence (in addition to microphysical properties of hydrometeors) may be an important factor for broadening the observed Doppler velocity range.

4.2. Event 2

4.2.1. Surface Precipitation

During Event 2, a strong discrepancy between simulations with different microphysical schemes can be noticed in terms of accumulated precipitation. Figure 7a shows that the simulations with the WDM6, Morrison, and Milbrandt schemes exhibit the best agreement with MRR and Pluvio2 observations while the simulations with the Thompson and P3 schemes strongly overestimate the accumulated precipitation (overestimation by more than 100% for P3). Fairly similar conclusions can be drawn when looking at the full domain-averaged accumulated precipitation or at the precipitation falling on the continental grid points of Adélie Land (Figure S4b). In particular, a patch of strong accumulation (>35 mm) a few kilometers west of DDU is visible in the P3 simulation (Figure S6).

In terms of precipitation type, almost all the surface precipitation at DDU in the Morrison and Thompson simulations is made of snow. In the WDM6 (resp. Milbrandt) simulation, 0.44 mm (resp. 3.12 mm) corresponding to 2.8% (resp. 21.4%) of the total amount falls as graupel. In the P3 simulations, 3.3% of the accumulated surface precipitation mass corresponds to rime (not shown).

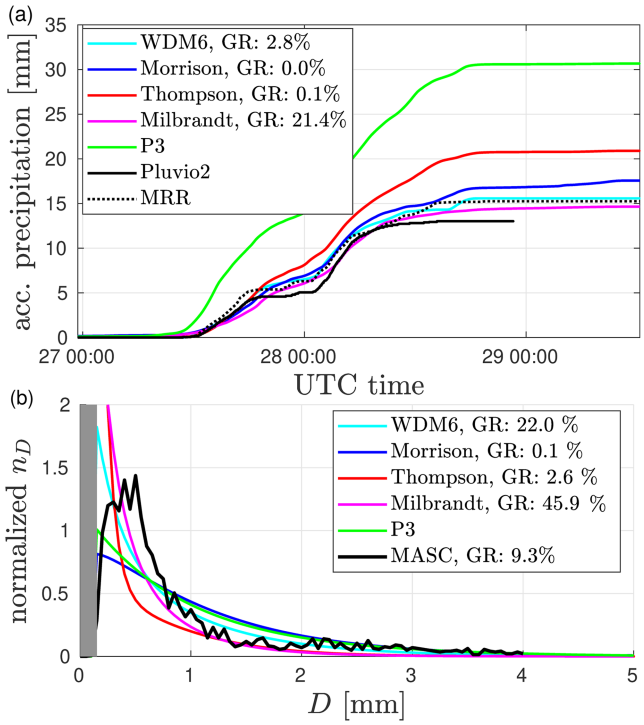

Figure 7. Same as Figure 4 but for Event 2. The Pluvio2 was dismounted on 29 January 2016, explaining the lack of data during this day. Mind the difference in *y* axis in panel a compared to Figure 4.

Looking at the surface precipitation PSD (Figure 7b), the WDM6, Morrison, and P3 schemes overestimate—relatively—the number of particles with $1 < D < 2$ mm compared to MASC data. Like for Event 1, the Thompson, Milbrandt, and WDM6 simulations overestimate the number of very small particles ($D < 0.5$ mm). Note that some cloud ice is present close to the surface during Event 2 in the WDM6 simulation. However, its contribution to the surface hydrometeor PSD cannot be taken into account since no ice PSD model is assumed in the WDM6 scheme. During Event 2, 9.3% of the MASC particles have been classified as graupel. Akin to Event 1, the Thompson and the Morrison simulations show a very weak quantity of graupel particles at the surface while the Milbrandt (resp. WDM6) have 45.9% (resp. 22.0%) of solid particles at the surface that corresponds to graupel. Simulated graupel particles mostly consist in particles with a dimension lower than 1 mm, enhancing the "hockey-stick" behavior of the Milbrandt's and WDM6's PSD curves as the diameter decreases.

4.2.2. Hydrometeor Mass Mixing Ratios

Figure 8 shows the averaged vertical profiles of the hydrometeor mass mixing ratios above DDU during Event 2. Alike Event 1, the simulation with the WDM6 scheme does not show any cloud liquid water. In addition, the WDM6 simulation presents a very different repartition of condensates—with much more cloud ice and less snow phase—compared to the simulations with the Morrison, Thompson, and Milbrandt schemes. All simulations but WDM6 show a peak of cloud liquid at $z \approx 1{,}500$ m, less pronounced in the Thompson simulation. At this altitude, the relative humidity with respect to liquid in the radiosonde on the 29 January at 00 UTC is very close to saturation (not shown). Below the cloud liquid water peak, the mass of rime start to increase with decreasing height in the P3 simulation (Figure 8a). One can further point out a second peak of cloud liquid water at $z \approx 4{,}000$ m in the Milbrandt simulation. This is explained by a slightly more pronounced air cooling at this altitude in the Milbrandt simulation during the event, making the relative humidity with respect to liquid water reaching saturation between 0415 and 1845 UTC on the 28 January. This second layer of cloud liquid water in Milbrandt is also located slightly above the beginning of the graupel generation (Figure 8a). While the graupel phase represents one quarter of the condensates mass at $z = 1{,}000$ m in the Milbrandt simulation, this phase is negligible in the Morrison and Thompson simulations. Similar observations can be made from the Polar WRF domain-averaged profiles (Figure S7). In the WDM6 simulation, graupel mixing ratios are small but not negligible near the surface (see inset in Figure 8a).

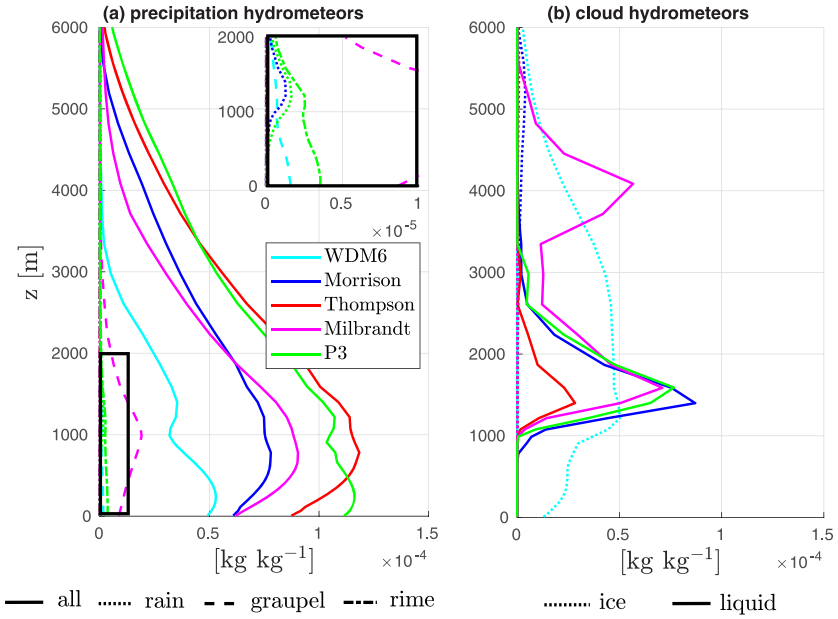

Figure 8. Same as Figure 5 but for Event 2. Mind differences in *x* axes compared to Figure 5.

Interestingly, Figure 8a shows that P3 and Thompson simulations—that is, the two simulations that strongly overestimate the surface precipitation—exhibit the highest mass mixing ratio peaks (at $z \approx 1{,}000$ m). One can also point out that unlike Event 1, the simulation of the low-level sublimation plays a less critical role in determining the surface precipitation. While the domain-averaged profiles of water vapor mixing ratios are similar in all the simulations (not shown), the differences in surface precipitation at DDU thus results from different geographical repartitions of the precipitation (see Figure S7) as well as discrepancies in clouds (ice and liquid) and precipitation formation specific to each scheme (see Figure S8 for the domain-averaged profiles).

4.2.3. Comparison to Radar: Vertical Profiles of Reflectivity and Doppler Velocity

Figure 9 shows the joint distributions of reflectivity and Doppler velocity during Event 2. Similarly to Event 1, MXPol and MRR shows reasonably similar distributions but MXPol detects more frequent low-reflectivity values than MRR due to its higher sensitivity. As a consequence, the median vertical profile of reflectivity in MXPol is nearly constant while that in MRR slightly increases with decreasing height. The modeled median reflectivity is fairly constant and realistic in the Morrison and Milbrandt simulations. A strong decrease with decreasing height below 1,000 m is noticeable in the Thompson simulation (and to a lesser extent in the P3 simulation). Although this decrease goes along with the behavior of the corresponding mass mixing ratios in Figure 8, it is not visible in the observed radar data. This points to a too low concentration of hydrometeors or too small snowflakes in the Thompson simulations, as suggested by Figure 7b. Interestingly, the joint distribution of the reflectivity in the Thompson simulation also shows a "two-branch" structure below 1,500 m, one branch corresponding to marked virgas at the beginning and end of Event 2 and the other one corresponding to the core of the event (see time-height plot in Figure S9). Such two-branch structure is however not present in radar data because observed virgas last during a shorter (cumulated) time. Furthermore, while the P3 simulation shows the highest cumulated precipitation, it does not exhibit reflectivity values higher than 20 dBZ, especially above 1,000 m of altitude. This suggests that particles simulated by P3 generally have a too small size.

Regarding the Doppler velocity, the overall shapes of the MRR and MXPol 2-D distributions are closer than during Event 1. Simulations show realistic values compared to observations. Like during Event 1, they all underestimate the variability compared to MRR and MXPol data. It is particularly evident for the Morrison and Milbrandt simulations that show a very narrow 80–20 interquantile range. Interestingly, the median velocity in the P3 simulation shows a monotonic increase with decreasing height and the 80th percentile is strongly overestimated below 1,500 m. The high Doppler velocity values are associated to highly rimed snowflakes at the beginning of the event. Indeed, between 00 and 06 UTC the 27 January 2016, the percentage of rime mass with respect to the mass of snowflakes can exceed 80% in this simulation.

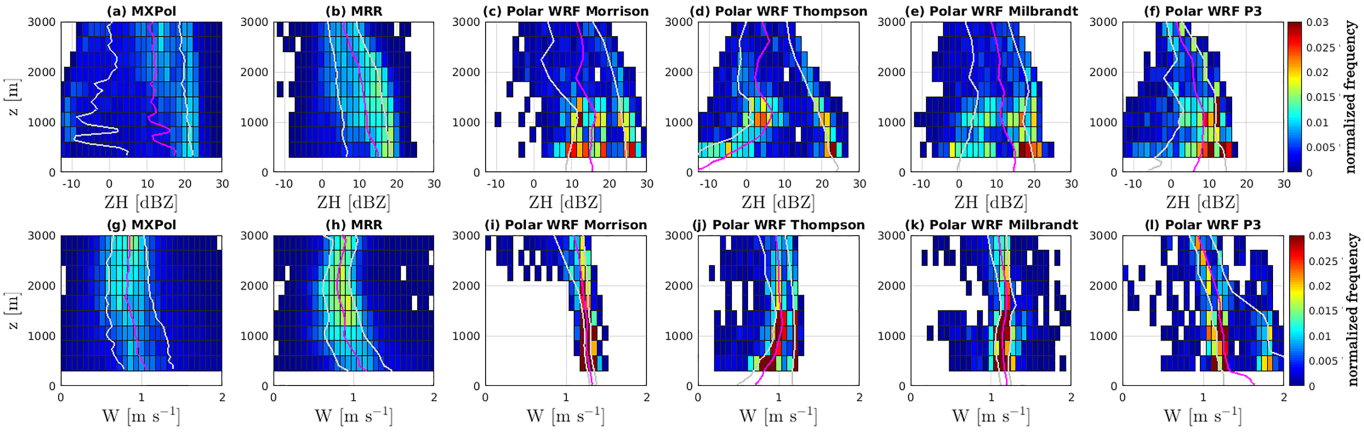

Figure 9. Same as Figure 6 but for Event 2.

5. Discussion on Key Microphysical Processes in Polar WRF Parameterizations

The comparison between Polar WRF simulations and the observations in the previous section made it possible to pinpoint deficiencies in the simulations in terms of precipitation amount, vertical structure of hydrometeors, and radar reflectivity. It also revealed substantial differences between the simulations with different (state-of-the-art) bulk microphysical schemes despite realistic and reasonably similar simulated profiles of temperature and humidity (see Appendix B). In this section, we discuss a few microphysical processes that play a critical role during the two precipitation events and whose different treatment by the parameterizations may explain the spread among the simulation results. The potential of radar polarimetry for further model evaluations is also discussed.

5.1. Cloud Condensates

When comparing the vertical profiles of mixing ratios, two striking observations were the absence of cloud liquid water in the WDM6 simulation and the very different repartition between cloud ice and snow in this simulation compared to those with the Morrison, Milbrandt, and Thompson schemes. Listowski and Lachlan-Cope (2017) already highlighted a deficit in supercooled liquid water in WDM6. The authors showed that this difference is due to the single-moment treatment of the cloud ice and to a lesser extent to a particularly high ice nuclei particle concentration. Moreover, the ice-snow autoconversion in WDM6 starts when the ice mixing ratio exceeds a critical value that corresponds to a mean ice diameter value of 500 μm (Hong et al., 2004). The definition of the ice and snow categories as well as the critical effective particle size impacting autoconversion is arbitrary and vary between microphysical schemes. Indeed, given the intrinsic complexity of the ice particles—with wide ranges of densitiy, size, and shape—defining different fixed iced hydrometeor categories and parameterizing autoconversion using an effective diameter threshold is a crude simplification of nature. The Thompson, Morrison, and Milbrandt schemes also use much lower values of the threshold diameter for autoconversion than in WDM6 (see section 2.2.2). This probably explains the particular repartition between the ice and snow categories in the latter scheme.

We previously noticed that the Milbrandt simulation shows a second peak of cloud droplet mass at z = 4,000 m during Event 2. This peak can be attributed to particularly cold temperatures at this altitude in this simulation that make the relative humidity with respect to liquid reaching the saturation during a few hours of 28 January 2018. Unfortunately, no measurement from the Cloud-Aerosol Lidar and Infrared Pathfinder Satellite Observations system (Vaughan et al., 2004) was available over the DDU region for the two studied events. Hence, we could not constrain the representation of cloud liquid water by observational data. However, the presence of supercooled liquid water above DDU is very probable given the detection of graupel particles at the surface by the MASC during the two events.

5.2. Growth of Snowflakes by Vapor Deposition and Aggregation

During Event 1 in the Morrison, Milbrandt, Thompson, and P3 simulations, the increase in snow mass mixing ratio from 6,000 to 2,000 m in absence (or quasi absence) of cloud ice and supercooled water (Figure 5) suggests that snowflakes grow by water vapor deposition during their fall. Such a conclusion also holds for the ice crystal class in the WDM6 simulation, and it is in agreement with the simulated supersaturated

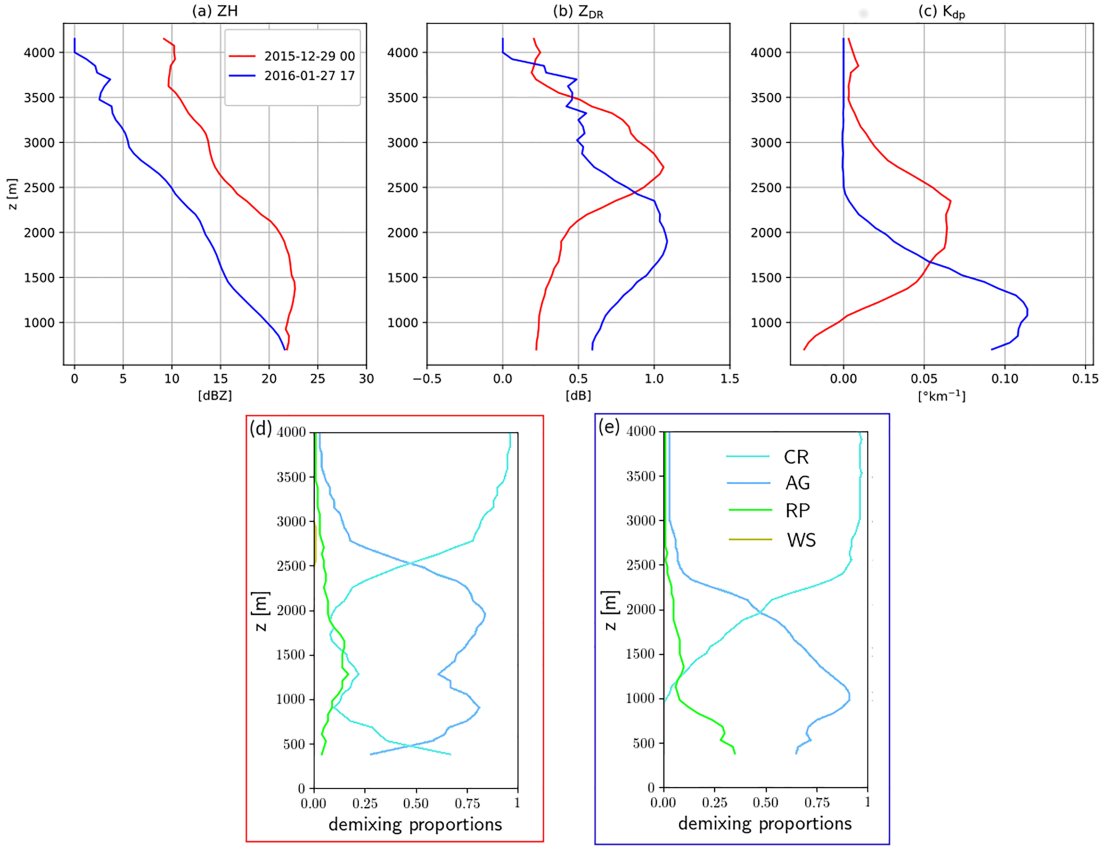

Figure 10. (a–c) Thirty-minute averaged vertical profiles of the reflectivity (a), Z_{DR} , and K_{dp} from MXPol during on 29 December 2015 at 00 UTC (reflectivity peak during Event 1, solid red lines) as well as on 27 January 2016 at 17UTC (first precipitation peak of Event 2, solid blue lines). (d and e) Thirty-minute averaged vertical profiles of the demixing proportions from MXPol data on 29 December 2015 at 00 UTC (panel d) and on 27 January 2016 at 17 UTC (panel f). In the legend, 'AG' stands for aggregates, "CR" for crystals, "RP" for rimed particles, and "WS" for wet snow. Note that all the plotted variables in this figure are averaged over all the radar volumes that are along the 203° RHI (about perpendicular to the coast), with a range lower than 20 km and whose elevation angle ranges between 4° (to avoid ground contamination) and 45° (to guarantee significant and meaningful polarimetric signature in the radar signal).

midtroposphere (Figure B1g). The same analysis can also be carried out for Event 2 in the 3,000- to 6,000-m altitude range (Figure 8) except for the Milbrandt simulation in which substantial supercooled liquid water is present and may induce snowflakes growth by riming (see next section). The absence of high reflectivity values (>20 dBZ) in the P3 and Thompson simulations above 1,000 m during Event 1 (Figure 6) suggests an underestimation of the concentration of relatively large snowflakes—those that affect the most the value of the reflectivity—during some parts of the event. This would concur with the underestimation of the number of large particles especially in the Thompson simulation compared to MASC data (Figure 4). The latter argument should however be interpreted with caution since the comparison with MASC data is made at the surface, that is, once a significant fraction of the precipitation has been sublimated.

Below 1,000 m, the temperature becomes warmer—roughly between −10 and 0° C during the two events—enhancing the efficiency of the aggregation process (Pruppacher & Klett, 1997). At the same time, the air becomes unsaturated, preventing the growth of snowflakes by vapor deposition. In the Morrison and Milbrandt simulations, we could point out during Event 1 in the first 1,000 m above the surface: (i) a strong decrease in the mass mixing ratio of snow (and graupel); (ii) an unrealistic (compared to radar data) absence of sharp decrease in reflectivity and an overestimation of its magnitude; (iii) an increase in mean mass diameter, which does not occur in the P3 and Thompson simulations (not shown). The latter three elements suggest that the self-collection by aggregation is too active in the katabatic layer in the Morrison and Milbrandt schemes (see Pasarelli & Srivastava, 1978, and Ferrier, 1994, for the aggregation parameterization in the Morrison and Milbrandt scheme, respectively). Note that a deficiency of the parameterization of the sublimation mechanism may also be pointed out (and may partly explain these observations) but it

would not be responsible for the overestimation of the reflectivity and the increase in mean mass diameter with decreasing height (see section 5.4).

5.3. Riming and Graupel Precipitation

During both events, the Milbrandt and P3 simulations—and to a lesser extent the Morrison simulation during Event 2—exhibit clear signs of riming below 2,000 m with either the production of graupel in the Milbrandt and Morrison simulations or with the increase in rime mass with decreasing height in P3. One may further suspect an excess of riming during Event 2 in P3 (particularly at the beginning of the event) because of the overestimated simulated Doppler velocities between 0 and 2,000 m of altitude (bottom row in Figure 9).

During the two events, the MASC also detected graupel particles at the surface. In terms of precipitation types in model simulations, only the Milbrandt scheme produces substantial graupel mixing ratios as well as graupel precipitation, especially during Event 2 (21.4% in mass). The comparison between the proportions (in number) of graupel particles detected by the MASC and those in simulations is delicate since the definition and distinction of graupel particles is, by essence, different in the model and in the MASC classification. However, the presence of a significant quantity of graupel near the surface in the Milbrandt simulation is qualitatively realistic.

5.4. Sublimation

Low-level sublimation is particularly marked during Event 1, with a radar reflectivity and simulated snow mixing ratios that strongly decrease with decreasing height in the first kilometer above the surface. From the decrease in observed reflectivity in MXPol and MRR data (Figure 6), we can infer a diminution of the size of the biggest snowflakes—that is, those that affect the most the radar signal—during their fall in the katabatic layer. In addition, the MASC PSD during Event 1 (see Figure 4) shows a decrease in the concentration of particles with a small diameter (≈0.5 mm). This decrease may have various causes, but one may reasonably conjecture about the preferential depletion of very small particles due to their weaker fall velocity—and subsequent higher ventilation time—as well as to their higher area to volume ratio (see details in Pruppacher & Klett, 1997, pp. 550–560). A similar effect is well known for the evaporation of rain drops (e.g., Kumjian & Ryzhkov, 2010). In the Polar WRF bulk microphysical schemes, the sublimation of solid particles is parameterized by diffusional mass and heat balance including ventilation effects (Ferrier, 1994; Morrison et al., 2005; Morrison & Grabowski, 2008; Pruppacher & Klett, 1997; Rutledge & Hobbs, 1983). The term describing the change in mass mixing ratio associated to sublimation is integrated over the size spectrum, and in the two-moment schemes, the reduction of the ice, graupel, and snow number concentration is scaled to the change in mass mixing ratio. This is equivalent to assuming a constant mean mass diameter (Morrison & Milbrandt, 2015). The predefined PSD model (gamma or inverse exponential) is of course not changed during this process. As the snow and graupel classes in the WDM6, Morrison, Thompson, and Milbrandt simulation are parameterized with an inverse-exponential (or superexponential) function and as no back-transfer to the cloud ice phase is simulated, a preferential depletion of small particles by sublimation cannot be properly represented in this schemes. One can actually point out that in the simulations that show the most intense sublimation effect during Event 1 (Thompson, P3, and WDM6; see Figure 5), the relative number of particles smaller (resp. higher) than ≈0.5 mm is overestimated (resp. underestimated) compared to MASC data (cf. Figure 4). This effect may partly explain the underestimation of the total amount of precipitation in these simulations because large particles (that contribute the most to the precipitation mass flux and that are in principle the less affected by sublimation) are probably excessively depleted. Further studies investigating the evolution of the snow PSD during the sublimation process, using, for example, simulations with spectral-bin microphysical schemes, could provide additional insights into this question.

5.5. The Potential of Radar Polarimetry for Characterizing Microphysical Processes and for Evaluating Their Representation in Model Simulations

The present simulation evaluation has been conducted without considering the comparison between observed and simulated polarimetric radar variables owing to the inability of the current radar simulator—at least with the current setting over our two study cases—to properly simulate the polarimetric quantities. However, it is worth claiming that the analysis of polarimetric quantities in MXPol data can substantially help in identifying the occurrence of microphysical processes. As a matter of fact, Figure 10 shows the vertical profiles of the reflectivity (Figure 10a), of the differential reflectivity (Z_{DR}, Figure 10b) and of the specific

differential phase shift on propagation (K_{dp}, Figure 10c) during one key period of Event 1 (peak of reflectivity during the event, red lines) and during one key period of Event 2 (first peak of precipitation, blue lines). Both the reflectivity and Z_{DR} increase with decreasing height in the upper part of the profiles. This suggests a snow growth mechanism that exacerbates the particle asymmetry like the dendritic growth by vapor deposition (Kennedy & Rutledge, 2011; Moisseev et al., 2015). For Event 1, this is in agreement with the supersaturation of the corresponding layer as well as temperatures around −15° C (see Figures 2g and 2h), that is, in the range of maximum dendritic growth efficiency (Hobbs et al., 1974). Below the altitude range where it increases with decreasing height, Z_{DR} starts to decrease while the reflectivity continue to increase indicating a process that makes the biggest particles—which Z_{DR} is sensitive to—less oblate. In addition, the Z_{DR} peak sits on top of a peak—and then a decrease with decreasing height—in K_{dp}. Such an evolution in the Z_{DR} and K_{dp} profiles is a characteristic of the aggregation process with the formation of oblate early aggregates of relatively small-to-medium size (a few mm; see Moisseev et al., 2015).

Figures 10d and 10e show the vertical profiles of the demixing proportions (estimated by the method of Besic et al., 2018) of four hydrometeor types corresponding to the two stages plotted in Figures 10a and 10c. One can notice that the increase in aggregate proportion—and decrease in crystal proportion—with decreasing height goes along with the decrease in Z_{DR} for both events in Figures 10b. One can also point out the significant proportion of rimed hydrometeors near the surface on 27 January 2016 at 17 UTC (Figures 10e) that concurs with the production of rime or graupel in the P3, Milbrandt, and WDM6 simulations during Event 2.

Nevertheless, a proper evaluation of simulations using the polarimetric information cannot rely on the comparison of instantaneous profiles that can suffer from differences in timing between simulations and observations. Such an evaluation requires the development of metrics whose temporal statistics can then be compared between simulations and radar observations. One may for instance suggest the derivation of descriptors for the height and depth of the dendritic growth layer or of the aggregation layer. This is beyond the scope of the present paper, and future works by the authors will focus on this aspect. Note that some work considering the application of the demixing method on simulation outputs—via the use of the radar simulator—is also under way. This would make it possible to compare similar hydrometeor proportions from both radar and model data.

6. Summary and Conclusions

This article addresses the representation of the microphysics of Antarctic precipitation in the atmospheric model Polar WRF. Simulations with different state-of-the-art microphysical schemes have been compared to surface and radar observations during two distinct and significant precipitation cases over coastal Adélie Land in summer. The main conclusions of the study are the following:

1. Notwithstanding the constrained large-scale dynamics and the robustness and realism of the modeled baseline meteorological variables fields, the amount of surface precipitation and the vertical structure of hydrometeor concentrations strongly depend upon the choice of the microphysical scheme. At DDU during Event 1, all the simulations underestimate the surface precipitation by several tens of percents especially when using the P3, Thompson, and WDM6 microphysical schemes. During Event 2, the Thompson and P3 simulations show the poorest performances with a strong overestimation of the accumulated precipitation exceeding 100% for P3. Regarding the hydrometeor types, only the Milbrandt scheme produces a substantial amount of graupel while the rest of the precipitation is in the snow (or ice) phase. This is consistent with the detection of graupel particles by the MASC.
2. The comparison of the simulations with radar and MASC data—via the use of simulators—has made it possible to pinpoint the critical microphysical processes involved during the two precipitation events and to assess their representation by the different microphysical schemes. During Event 1, the amount of surface precipitation strongly depends on the low-level sublimation. It is very likely that the current coarse treatment of the sublimation process in the microphysical parameterizations is responsible—at least partly—for the underestimation of the surface precipitation. The comparison of the vertical structure of simulated and observed reflectivity also suggests that aggregation is too active within the katabatic layer in the Morrison simulation and—to a lesser extent—in the Milbrandt simulation during Event 1. During the two events and particularly during Event 2, supercooled liquid water is present above DDU, and snowflake growth by riming is active. Concurring with the study of Listowski and Lachlan-Cope (2017),

the WDM6 scheme does not produce a significant amount of supercooled liquid water during the two events, and it further shows a very different repartition of cloud ice and snow condensates compared to the other microphysical schemes. On the other hand, Milbrandt and P3 simulations show clear signals of riming with the generation of graupel or rime mass.

None among the tested state-of-the-art microphysical schemes give very satisfactory results in terms of precipitation amount, radar signatures, and hydrometeors PSDs, and none of them perform significantly better than the others, but the Milbrandt scheme gives the most correct cumulated precipitation during the two events. It would thus be improper from our current results to unreservedly recommend the usage of one specific microphysical scheme for future weather or climate simulations over Antarctica with Polar WRF. It is worth mentioning that the dependency of the model performance upon the model resolution has not been addressed in the present paper, and further work should tackle this issue. For simulations at lower resolution than 1 km, one may consider not only different microphysical schemes but also macrophysical aspects, that is, the subgrid variability of cloud and precipitation. The comparison of the simulations with observational data has however made it possible to pinpoint shortcomings in all the microphysical parameterizations. This may help in the interpretation of future simulations of precipitation over polar regions and invites for future parameterization assessments and developments particularly regarding the description of the PSD and the sublimation process. A more comprehensive evaluation of the Polar WRF microphysical schemes in the Antarctic context would require more study cases, in all seasons and in various regions of the ice sheet. Further observational data, giving also access to clouds characteristics, covering the winter season and ideally considering different Antarctic regions would be very helpful for this purpose. It should be noted that such data are not yet available. Moreover, this paper has also discussed the potential of the radar polarimetry and of the demixing method to identify and locate the occurrence of microphysical processes like growth by vapor deposition and aggregation. These aspects should be further explored in a model evaluation framework. Finally, as this paper sheds light on the strong dependency of the amount and structure of Antarctic precipitation upon the choice of the microphysical scheme, it invites to a thorough sensitivity study to the microphysical scheme and/or careful tuning of the microphysics in climate models used for polar studies. This seems to be a necessary step for correctly interpreting the simulation of the current and future mass balance of the ice sheets.

Appendix A: Detailed Description of the MASC Simulator

We assume a virtual MASC in Polar WRF set at the first model level at the DDU grid point. At a time t, the vertical flux F_D of particles of type i and of diameter D through the sampling surface $S = 8.3\text{cm}^2$ of the MASC reads as follows:

$$F_D^i(t) = \rho_a(t)\left(w(t) + \omega_D^i(t)\right) N_D^i(t) S, \tag{A1}$$

where w is the vertical velocity of the local flow, ω_D^i is the fall velocity of i-type particles in a flow at rest, ρ_a the air density, and N_D^i the number mixing ratio of i-type particles of diameter D per kilogram of air. For convenience, we orient here the vertical axis z toward the ground surface, such as ω_D is positive.

During a sampling period Δt, the number of i-type particles that fall through S reads as follows:

$$n_D^i = \int_t^{t+\Delta t} \rho_a(t)\left(w(t) + \omega_D^i(t)\right) N_D^i(t) S dt. \tag{A2}$$

In the model, the vertical velocity w can be decomposed as the sum of a slowly varying large-scale dynamical component w_d and a local (subgrid) turbulent part w_t. Hence,

$$n_D^i = \underbrace{\int_t^{t+\Delta t} \rho_a(t) N_D^i(t) w_d(t) S dt}_{(1)} + \underbrace{\int_t^{t+\Delta t} + \rho_a(t) N_D^i(t) w_t(t) S dt}_{(2)} + \underbrace{\int_t^{t+\Delta t} \rho_a(t) \omega_D^i(t) N_D^i(t) S dt}_{(3)}. \tag{A3}$$

Regarding the turbulent mixing of cloud and precipitation hydrometeors, the current version of Polar WRF only deals with the subgrid mixing of the mass mixing ratios of cloud ice and cloud droplets. As we mostly

focus on solid hydrometeors in free fall (mostly snow and graupel types), the second term of equation (A3) has thus been neglected. Equation (A3) thus reduces to

$$n_D^i = \int_t^{t+\Delta t} \rho_a(t) N_D^i(t) w_d(t) S dt + \int_t^{t+\Delta t} \rho_a(t) \omega_D^i(t) N_D^i(t) S dt. \quad \text{(A4)}$$

Polar WRF microphysical schemes assume inverse-exponential number distributions or gamma size distribution for hydrometeors. N_D^i can thus be estimated from the total number concentration and mixing ratio of the corresponding hydrometeor at the first model level. Likewise, the terminal fall velocities are diagnostic—that is, calculated with formulae of the form $\omega_D^i = \alpha_c D^{\beta_c} e^{-\gamma_c D}$, where α_c, β_c, and γ_c are three constants—such as ω_D^i can be calculated at each type step for each hydrometeor type.

As w_d is a prognostic variable of the model dynamics, equation (A4) can be directly solved from model outputs at the first model level at each time step. It is thus possible to compare the quantity n_D between the MASC and model simulations.

Appendix B: Standard Meteorological Variables in the Simulations

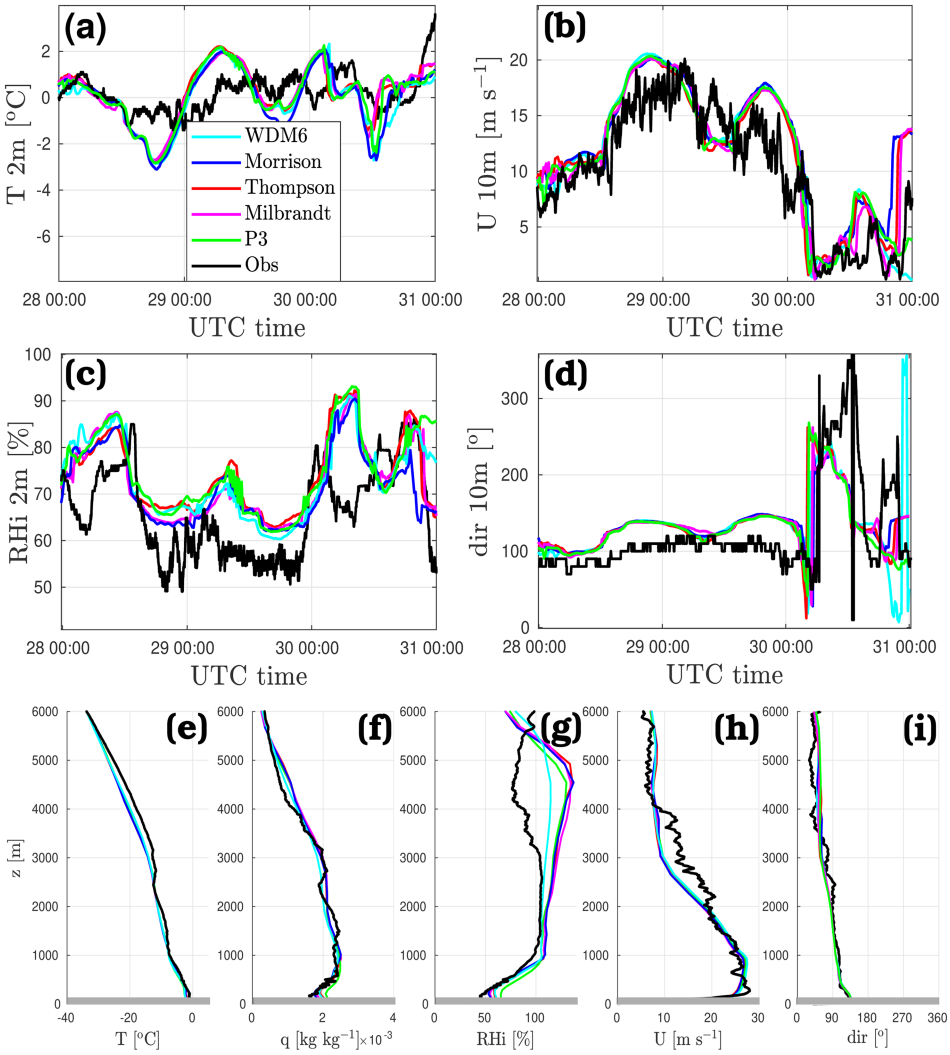

Figure B1. (a–d) Time series of the 2-m temperature (a), the 10-m wind speed (b), the 2-m relative humidity with respect to ice (c), and of the 10-m wind direction (d) at DDU during Event 1 in surface observations (black line) and Polar WRF simulations (colored lines). (e–i) Vertical profiles of the temperature (e), specific humidity (f), relative humidity with respect to ice (g), wind speed (h), and wind direction (i) above DDU on 29 December 2015 at 00 UTC from radiosonde data (black line) and Polar WRF simulations (colored line). Gray strips shade the first 100 m above the ground surface where radiosoudings are not reliable (Vignon et al., 2019).

Prior to compare simulations to radar and MASC observations and to infer conclusions about the representation of microphysical processes, one must ensure that the atmospheric dynamics around DDU is well captured—and the baseline meteorological variables well represented—by the model. Figures B1a–B1d (resp. Figures B2a–B2d) compare the time series of near-surface temperature, relative humidity, wind speed, and wind direction at DDU in the simulations and in the observation during Event 1 (resp. Event 2). Figures B1e–B1i compare the vertical profiles of temperature, specific and relative humidity, wind speed, and wind direction on 29 December 2015 at 00 UTC (resp. 28 January 2016 at 00 UTC), that is, during the middle phase of the event. One can first of all notice the overall fairly good agreement between simulations and observations and the weak discrepancies among the different simulations for all the variables during the two events. Note that although we compare here the vertical profiles with one radiosounding, similar agreement is found for the other radiosoundings covering the two events (not shown). This first conclusion makes us confident with the ability of the Polar WRF model at a 1-km resolution—and in the nested and nudged configuration presented in the main paper—to represent the regional dynamics around DDU during the two precipitation events and to provide realistic baseline meteorological variables. As the simulated temperature, specific humidity and wind fields agree with those observed, and as they do not significantly differ between simulations, we can be fairly confident to attribute most of differences of precipitation amount and structure to the microphysical scheme.

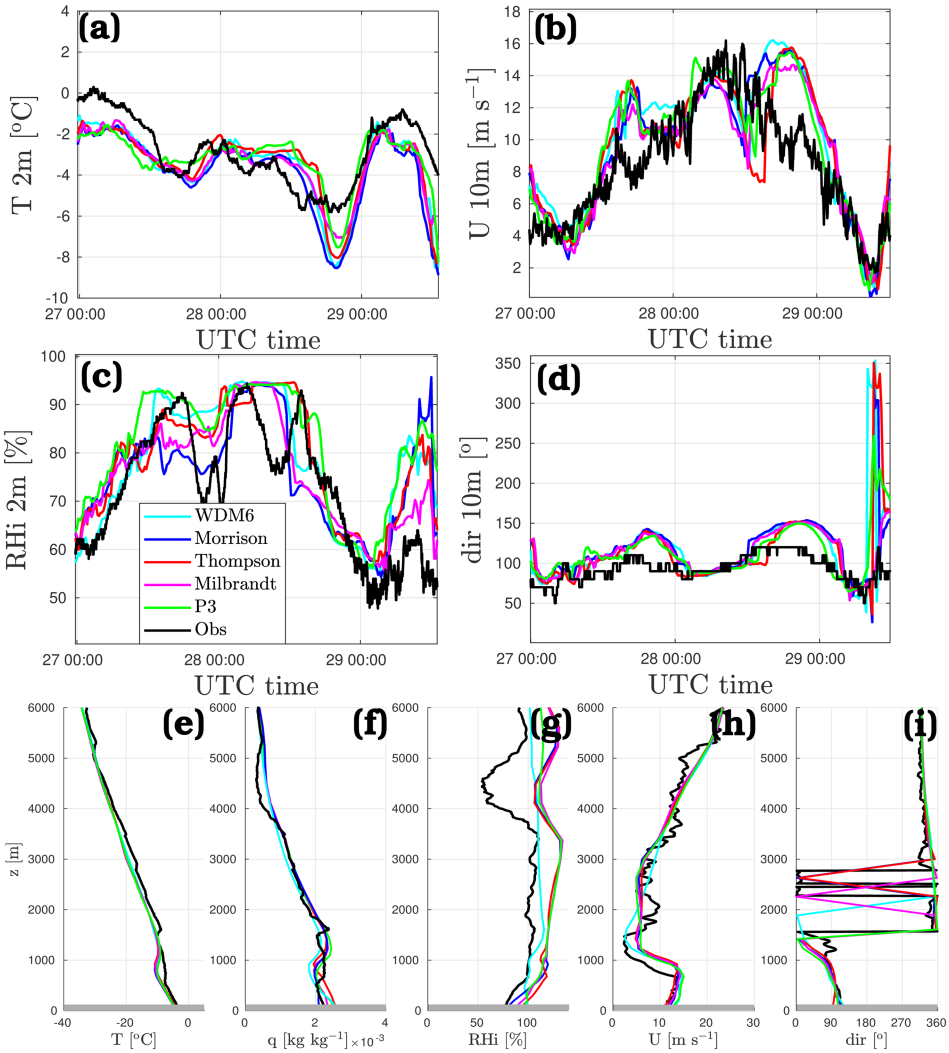

Figure B2. Same as Figure B1 but for the time series during Event 2 and for the vertical profiles on 28 January 2016 at 00 UTC.

If we now analyze more attentively Figure B1, we can notice a slightly too pronounced diurnal cycle of the 2-m temperature in the simulations. This can be mostly explained by an overestimated downward shortwave radiative flux during the daytime (in overcast conditions) in the simulations compared to observations (not shown). In Figure B1 one can also point out an overestimated near-surface relative humidity in the simulations. No clear explanation has been found for this bias but as the model mesh encompassing DDU contains a significant fraction of free ocean—in agreement with the visual observation of the sea ice conditions on the field—the mesh-averaged surface water flux toward the atmosphere may be overestimated, leading to larger near-surface humidity values compared to local measurements over the rocky Petrels Island. A careful look at Figure B2 also reveals that notwithstanding the correct specific humidity, the simulated vertical profile of relative humidity shows values higher than those observed. This is probably explained by the slightly colder simulated low-troposphere compared to radiosonde data.

Acknowledgments
This work was funded by the EPFL-LOSUMEA project. The contribution of J. Gehring was supported by the Swiss National Science Foundation under Grant 200020-175700. N. Besic's work was supported by MeteoSwiss. The authors thank Aleksandra Tatarevic and the Applied Radar Science Group for developing and freely distributing the CR-SIM radar simulator. The CR-SIM radar simulator is freely distributed online (at https://www.bnl.gov/CMAS/cr-sim.php). We are also thankful to A. Ferrone, C. Durán Alarcón, C. Praz, A. Reverdin, and M. Schaer for preprocessing radar and MASC data. We thank C. Genthon, G. Sotiropoulou, and J. Grazioli for insightful discussions. The APRES3 campaign data have been distributed on the PANGAEA data repository (https://www.pangaea.de,_https://doi.org/10.1594/PANGAEA.883562). A description of the data set is provided in Genthon et al. (2018). C Listowski is also thanked for providing the Bedmap2 data set for Polar WRF. The authors acknowledge the support of the French National Research Agency (ANR) and of the French Polar Institute through the APRES3 project. The authors appreciate the support of Météo-France, the DSO/DOA service, and Pascal Herrera for the acquisition and distribution of near-surface and radiosonde data at DDU station. We also thank Francisco Tapiador and two anonymous reviewers for their careful evaluation of the manuscript and thoughtful comments.

References

Agosta, C., Amory, C., Kittel, C., Orsi, A., Favier, V., Gallée, H., et al. (2019). Estimation of the antarctic surface mass balance using the regional climate model MAR (1979–2015) and identification of dominant processes. *The Cryosphere*, *13*(1), 281–296. https://doi.org/10.5194/tc-13-281-2019

Behrangi, A., Christensen, M., Richardson, M., Lebsock, M., Stephens, G., Huffman, G. J., et al. (2016). Status of high-latitude precipitation estimates from observations and reanalyses. *Journal of Geophysical Research: Atmospheres*, *121*, 4468–4486. https://doi.org/10.1002/2015JD024546

Besic, N., Figuera i Ventura, J., Grazioli, J., Gabella, M., Germann, U., & Berne, A. (2016). Hydrometeor classification through statistical clustering of polarimetric radar measurements: A semi-supervised approach. *Atmospheric Measurement Techniques*, *9*, 4425–4445. https://doi.org/10.5194/amt-9-4425-2016

Besic, N., Gehring, J., Praz, C., Figuera i Ventura, J., Grazioli, J., Gabella, M., et al. (2018). Unraveling hydrometeor mixtures in polarimetric radar measurements. *Atmospheric Measurement Techniques*, *11*, 4847–4866. https://doi.org/10.5194/amt-11-4847-2018

Bracegirdle, T. J., & Marshall, G. J. (2012). The reliability of antarctic tropospheric pressure and temperature in the latest global reanalyses. *Journal of Climate*, *25*(20), 7138–7146. https://doi.org/10.1175/JCLI-D-11-00685.1

Bromwich, D. H., Otieno, F. O., Hines, K. M., Manning, K. W., & Shilo, E. (2013). Comprehensive evaluation of polar weather research and forecasting model performance in the antarctic. *Journal of Geophysical Research: Atmospheres*, *118*, 274–292. https://doi.org/10.1029/2012JD018139

Cohard, J.-M, & Pinty, J.-P (2000). A comprehensive two-moment warm microphysical bulk scheme. I: Description and tests. *Quarterly Journal of the Royal Meteorological Society*, *126*(566), 1815–1842. https://doi.org/10.1002/qj.49712656613

Deb, P., Andrew, O., Scott, H. J., Tony, P., John, T., Daniel, B., et al. (2016). An assessment of the polar weather research and forecasting (WRF) model representation of near-surface meteorological variables over west antarctica. *Journal of Geophysical Research: Atmospheres*, *121*, 1532–1548. https://doi.org/10.1002/2015JD024037

Del Guasta, M., Morandi, M., Stefanutti, L., Brechet, J., & Piquad, J. (1993). One-year of cloud lidar data from Dumont d'Urville (Antarctica). 1. General overview of geometrical and optical properties. *Journal Geophysical Research*, *98*, 18,575–18,587. https://doi.org/10.1029/93JD01476

Durán-Alarcón, C., Boudevillain, B., Genthon, C., Grazioli, J., Souverijns, N., van Lipzig, N. P. M., et al. (2019). The vertical structure of precipitation at two stations in East Antarctica derived from Micro Rain Radars. *The Cryosphere*, *3*(1), 247–264. https://doi.org/10.5194/tc-13-247-2019

Favier, V., Agosta, C., Parouty, S., Durand, G., Delaygue, G., Gallee, H., et al. (2013). An updated and quality controlled surface mass balance dataset for Antarctica. *The Cryosphere*, *7*(2), 583–597. https://doi.org/10.5194/tc-7-583-2013

Ferrier, B. S. (1994). A double-moment multiple-phase four-class bulk ice scheme. Part I: Description. *Journal of the Atmospheric Sciences*, *51*, 249–280.

Fretwell, P. (2013). Bedmap2: Improved ice bed, surface and thickness datasets for Antarctica. *The Cryosphere*, *7*(1), 375–393. https://doi.org/10.5194/tc-7-375-2013

Garrett, T. J., Fallgatter, C., Shkurko, K., & Howlette, D. (2012). Fall speed measurement and high resolution multi-angle photography of hydrometeors in free fall. *Atmospheric Measurement Techniques*, *5*, 2625–2633. https://doi.org/10.5194/amt-5-2625-2012

Gedzelman, S. D., & Arnold, R. (1994). Modeling the isotopic composition of precipitation. *Journal of Geophysical Research*, *99*, 10,455–10,471. https://doi.org/10.1029/93JD03518

Genthon, C., Berne, A., Grazioli, J., Durán-Alarcón, C., Praz, C., & Boudevillain, B. (2018). Precipitation at Dumont d'Urville, Adélie Land, East Antarctica: The APRES3 field campaigns dataset. *Earth System Science Data*, *10*, 1605–1612. https://doi.org/10.5194/essd-10-1605-2018

Genthon, C., Krinner, G., & Castebrunet, H. (2009). Antarctic precipitation and climate-change predictions: horizontal resolution and margin vs plateau issues. *Annals Glaciology*, *50*, 55–60.

Genthon, C., Krinner, G., & Sacchettini, M. (2003). Interannual Antarctic tropospheric circulation and precipitation variability. *Climate Dynamics*, *21*, 289–307. https://doi.org/10.1007/s00382-003-0329-1

Gerber, F., Besic, N., Sharma, V., Mott, R., Daniels, M., Gabella, M., et al. (2018). Spatial variability in snow precipitation and accumulation in COSMO-WRF simulations and radar estimations over complex terrain. *The Cryosphere*, *12*(10), 3137–3160. https://doi.org/10.5194/tc-12-3137-2018

Gorodetskaya, I. V., Kneifel, S., Maahn, M., Van Tricht, K., Thiery, W., Schween, J. H., et al. (2015). Cloud and precipitation properties from ground-based remote-sensing instruments in east antarctica. *The Cryosphere*, *9*(1), 285–304. https://doi.org/10.5194/tc-9-285-2015

Grazioli, J., Genthon, C., Boudevillain, B., Duran-Alarcon, C., Del Guasta, M., Madeleine, J.-B., & Berne, A. (2017). Measurements of precipitation in Dumont d'Urville, Adélie Land, East Antarctica. *The Cryosphere*, *11*(4), 1797–1811. https://doi.org/10.5194/tc-11-1797-2017

Grazioli, J., Madeleine, J.-B., Gallée, H., Forbes, R. M., Genthon, C., Krinner, G., & Berne, A. (2017). Katabatic winds diminish precipitation contribution to the Antarctic ice mass balance. *Proceedings of the National Academy of Sciences*, *114*(41), 10,858–10,863. https://doi.org/10.1073/pnas.1707633114

Hines, K. M., & Bromwich, D. H. (2008). Development and testing of polar Weather Research and Forecasting (WRF) model. Part I: Greenland Ice Sheet Meteorology. *Monthly Weather Review*, *136*(6), 1971–1989. https://doi.org/10.1175/2007MWR2112.1

Hines, K. M., & Bromwich, D. H. (2017). Simulation of late summer Arctic clouds during ASCOS with Polar WRF. *Monthly Weather Review*, *145*(2), 521–541. https://doi.org/10.1175/MWR-D-16-0079.1

Hines, K. M., Bromwich, D. H., Bai, L., Bitz, C. M., Powers, J. G., & Manning, K. W. (2015). Sea ice enhancements to Polar WRF. *Monthly Weather Review*, *143*(6), 2363–2385. https://doi.org/10.1175/MWR-D-14-00344.1

Hines, K. M., Bromwich, D. H., Wang, S.-H., Silber, I., Verlinde, J., & Lubin, D. (2019). Microphysics of summer clouds in central West Antarctica simulated by the Polar Weather Research and Forecasting Model (WRF) and the Antarctic Mesoscale Prediction System (AMPS). *Atmospheric Chemistry and Physics Discussions*, *19*, 12,431–12,454. https://doi.org/10.5194/acp-19-12431-2019, 2019

Hobbs, P. V., Chang, S., & Locatelli, J. D. (1974). The dimensions and aggregation of ice crystals in natural clouds. *Journal of Geophysical Research*, *79*, 2199–2206.

Hong, S.-Y., Dudhia, J., & Chen, S.-H. (2004). A revised approach to ice microphysical processes for the bulk parametrization of clouds and precipitation. *Monthly Weather Review*, *132*, 103–120. https://doi.org/10.1175/1520-0493(2004)132<0103:ARATIM>2.0.CO;2

Huang, G.-J., Kleinkort, C., Bringi, V. N., & abd Notaroš, B. N. (2017). Winter precipitation particle size distribution measurement by Multi-Angle Snowflake Camera. *Atmospheric Research*, *198*, 81–96. https://doi.org/10.1016/j.atmosres.2017.08.005

Kennedy, P. C., & Rutledge, S. A. (2011). S-band dual-polarization radar observations of winter storms. *Journal of Applied Meteorology and Climatology*, *50*(4), 844–858. https://doi.org/10.1175/2010JAMC2558.1

King, J. C., Gadian, A., Kirchgaessner, A., Kuipers Munneke, P., Lachlan-Cope, T. A., Orr, A., et al. (2015). Validation of the summertime surface energy budget of Larsen C ice shelf (Antarctica) as represented in three high-resolution atmospheric models. *Journal of Geophysical Research: Atmospheres*, *120*, 1335–1347. https://doi.org/10.1002/2014JD022604

Kittel, C., Amory, C., Agosta, C., Delhasse, A., Doutreloup, S., Huot, P.-V., et al. (2018). Sensitivity of the current Antarctic surface mass balance to sea surface conditions using Mar. *The Cryosphere*, *12*(12), 3827–3839. https://doi.org/10.5194/tc-12-3827-2018

Krinner, G., Largeron, C., Ménégoz, M., Agosta, C., & Brutel-Vuilmet, C. (2014). Oceanic forcing of Antarctic climate change: A study using a stretched-grid atmospheric general circulation model. *Journal of Climate*, *27*, 5786–5800. https://doi.org/10.1175/JCLI-D-13-00367.1

Kumjian, M. R., & Ryzhkov, A. V. (2010). The impact of evaporation on polarimetric characteristics of rain: Theoretical model and practical implications. *Journal of Applied Meteorology and Climatology*, *49*(6), 1247–1267. https://doi.org/10.1175/2010JAMC2243.1

Lemonnier, F., Madeleine, J.-B., Claud, C., Genthon, C., Durán-Alarcón, C., Palerme, C., et al. (2019). Evaluation of CloudSat snowfall rate profiles by a comparison with in situ Micro-Rain Radar observations in East Antarctica. *The Cryosphere*, *13*(3), 943–954. https://doi.org/10.5194/tc-13-943-2019

Lenaerts, J. T. M., Fyke, J., & Medley, B. (2018). The signature of ozone depletion in recent antarctic precipitation change: A study with the Community Earth System model. *Geophysical Research Letters*, *45*, 12,931–12,939. https://doi.org/10.1029/2018GL078608

Lenaerts, JanT. M., Vizcaino, M., Fyke, J., van Kampenhout, L., & van den Broeke, M. R. (2016). Present-day and future Antarctic ice sheet climate and surface mass balance in the community earth system model. *Climate Dynamics*, *47*(5), 1367–1381. https://doi.org/10.1007/s00382-015-2907-4

Li, J-LF, Richardson, M., Hong, Y., Lee, W.-L., Wang, Y.-H., Yu, J.-Y., et al. (2017). Improved simulation of antarctic sea ice due to the radiative effects of falling snow. *Environmental Research Letters*, *12*(8), 84010. https://doi.org/10.1088/1748-9326/aa7a17

Lim, K.-S., & Hong, S.-Y. (2010). Development of en effective double-moment cloud microphysics scheme with prognostics cloud condensation nuclei (CCN) for weather and climate model. *Monthly Weather Review*, *138*, 1587–1612. https://doi.org/10.1175/2009mwr2968.1

Listowski, C., Delanoë, J., Kirchgaessner, A., Lachlan-Cope, T., & King, J. (2019). Antarctic clouds, supercooled liquid water and mixed phase, investigated with DARDAR: Geographical and seasonal variations. *Atmospheric Chemistry and Physics*, *19*(10), 6771–6808. https://doi.org/10.5194/acp-19-6771-2019

Listowski, C., & Lachlan-Cope, T. (2017). The microphysics of clouds over the Antarctic peninsula—Part 2: Modelling aspects within Polar WRF. *Atmospheric Chemistry and Physics*, *17*(17), 10,195–10,221. https://doi.org/10.5194/acp-17-10195-2017

Maahn, M., & Kollias, P. (2012). Improved Micro Rain Radar snow measurements using Doppler spectra post-processing. *Atmospheric Measurement Techniques*, *5*(11), 2661–2673. https://doi.org/10.5194/amt-5-2661-2012

Marshall, G. J., Thompson, DavidW. J., & van den Broeke, M. R. (2017). The signature of southern hemisphere atmospheric circulation patterns in Antarctic precipitation. *Geophysical Research Letters*, *44*, 11,580–11,589. https://doi.org/10.1002/2017GL075998

Milbrandt, J. A., & Morrison, H. (2016). Parameterization of cloud microphysics based on the prediction of bulk ice particle properties. Part III: Introduction of multiple free categories. *Journal of the Atmospheric Sciences*, *73*(3), 975–995. https://doi.org/10.1175/JAS-D-15-0204.1

Milbrandt, J. A., & Yau, M. K. (2005). A multimoment bulk microphysics parameterization. Part I: Analysis of the role of the spectral shape parameter. *Journal of the Atmospheric Sciences*, *62*, 3051–3064. https://doi.org/10.1175/JAS3534.1

Min, K.-H., Choo, S., Lee, D., & Lee, G. (2015). Evaluation of WRF Cloud Microphysics Schemes Using Radar Observations. *Weather and Forecasting*, *30*(6), 1571–1589. https://doi.org/10.1175/WAF-D-14-00095.1

Moisseev, D. N., Lautaportti, S., Tyynela, J., & Lim, S. (2015). Dual-polarization radar signatures in snowstorms: Role of snowflake aggregation. *Journal of Geophysical Research: Atmospheres*, *120*, 12,644–12,655. https://doi.org/10.1002/2015JD023884

Monaghan, A. J., Bromwich, D. H., & Schneider, D. P. (2008). Twentieth century antarctic air temperature and snowfall simulations by IPCC climate models. *Geophysical Research Letters*, *35*, L07502. https://doi.org/10.1029/2007GL032630

Morrison, H., Curry, D. A., & Khvorostyanov, V. I. (2005). A new double-moment microphysics parametrization for application in cloud and climate models. Part I: Description. *Journal of the Atmospheric Sciences*, *62*, 1665–1677. https://doi.org/10.1175/jas3446

Morrison, H., & Grabowski, W. W. (2008). A novel approach for representing ice microphysics in models: Description using a kinematic framework. *Journal of the Atmospheric Sciences*, *65*, 1528–1548. https://doi.org/10.1175/2007JAS2491.1

Morrison, H., & Milbrandt, J. A. (2015). Parameterization of cloud microphysics based on the prediction of bulk ice particle properties. Part I: Scheme description and idealized tests. *Journal of the Atmospheric Sciences*, *72*(1), 287–311. https://doi.org/10.1175/JAS-D-14-0065.1

Morrison, H., Thompson, G., & Tatarskii, V. (2009). Impact of cloud microphysics on the development of trailing stratiform precipitation in a simulated squall line: Comparison of one- and two-moment schemes. *Monthly Weather Review*, *137*(3), 991–1007. https://doi.org/10.1175/2008MWR2556.1

Nicholls, S. D., Decker, S. G., Tao, W.-K., Lang, S. E., Shi, J. J., & Mohr, K. I. (2017). Influence of bulk microphysics schemes upon Weather Research and Forecasting (WRF) Version 3.6.1 nor'easter simulations. *Geoscientific Model Development*, *10*(2), 1033–1049. https://doi.org/10.5194/gmd-10-1033-2017

Palerme, C., Genthon, C., Claud, C., Kay, J. E., Wood, N. B., & L'Ecuyer, T. (2017). Evaluation of current and projected Antarctic precipitation in CMIP5 models. *Climate Dynamics*, *48*(1), 225–239. https://doi.org/10.1007/s00382-016-3071-1

Palerme, C., Kay, J. E., Genthon, C., L'Ecuyer, T., Wood, N. B., & Claud, C. (2014). How much snowfalls on the Antarctic icesheet. *The Cryosphere*, *8*, 1577–1587. https://doi.org/10.5194/tc-8-1577-2014

Pasarelli, R. E., & Srivastava, R. C. (1978). A new aspect of snowflake aggregation theory. *Journal of the Atmospheric Sciences*, *36*, 484–493.

Praz, C., Roulet, Y-A., & Berne, A. (2017). Solid hydrometeor classification and riming degree estimation from pictures collected with a Multi Angle Snowflake Camera. *Atmospheric Measurement Techniques*, *10*, 1335–1357. https://doi.org/10.5194/amt-10-1335-2017

Previdi, M., & Polvani, L. M. (2016). Anthropogenic impact on antarctic surface mass balance, currently masked by natural variability, to emerge by mid-century. *Environmental Research Letters*, *11*(9), 94001. Retrieved from http://stacks.iop.org/1748-9326/11/i=9/a=094001

Pruppacher, H. R., & Klett, J. D. (1997). *Microphysics of clouds and precipitation* (2nd ed., p. 954). Dordrecht: Kluwer Academic.

Rutledge, S. A., & Hobbs, P. (1983). The mesoscale and microscale structure and organization of clouds and precipitation in midlatitude cyclones. VIII: A model for the seeder-feeder process in warm-frontal rainbands. *Journal of the Atmospheric Sciences*, *40*(5), 1185–1206. https://doi.org/10.1175/1520-0469(1983)040h1185:TMAMSAi2.0.CO;2

Schaer, M., Praz, C., & Berne, A. (2018). Identification of blowing snow particles in images from a multi-angle snowflake camera. *The Cryosphere Discussions*, *2018*, 1–23. https://doi.org/10.5194/tc-2018-248

Schneebeli, M., Dawes, N., Lehning, M., & Berne, A. (2013). High- resolution vertical profiles of polarimetric X-band weather radar observables during snowfall in the Swiss Alps. *J Appl Meteorol Clim*, *52*, 378–394. 10.1175/JAMC-D-12-015.1.

Souverijns, N., Gossart, A., Lhermitte, S., Gorodetskaya, I. V., Grazioli, J., Berne, A., et al. (2018). Evaluation of the CloudSat surface snowfall product over Antarctica using ground-based precipitation radars. *The Cryosphere*, *12*(12), 3775–3789. https://doi.org/10.5194/tc-12-3775-2018

Straka, J. M. (2009). *Cloud and precipitation microphysics: Principles and parameterizations*: Cambridge University Press.

Tapiador, F. J., Roca, R., Genio, A. D., Dewitte, B., Petersen, W., & Zhang, F. (2018). Is precipitation a good metric for model performance? *Bulletin of the American Meteorological Society*, *100*, 223–233. https://doi.org/10.1175/BAMS-D-17-0218.1

Tapiador, F. J., Sánchez, J.-L., & García-Ortega, E. (2019). Empirical values and assumptions in the microphysics of numerical models. *Atmospheric Research*, *215*, 2014–238. https://doi.org/10.1016/j.atmosres.2018.09.010

The IMBIE team (2018). Mass balance of the Antarctic Ice Sheet from 1992 to 2017. *Nature*, *558*, 219–235. https://doi.org/10.1038/s41586-018-0179-y

Thomas, E. R., van Wessem, J. M., Roberts, J., Isaksson, E., Schlosser, E., Fudge, T. J., et al. (2017). Regional antarctic snow accumulation over the past 1000 years. *Climate of the Past*, *13*(11), 1491–1513. https://doi.org/10.5194/cp-13-1491-2017

Thompson, G., & Eidhammer, T. (2014). A study of aerosol impacts on clouds and precipitation development in a large winter cyclone. *Journal of the Atmospheric Sciences*, *71*(10), 3636–3658. https://doi.org/10.1175/JAS-D-13-0305.1

Thompson, G., Field, P. R., Rasmussen, R. M., & Hall, W. D. (2008). Explicit forecasts of winter precipitation using an improved bulk microphysics scheme. Part II: Implementation of a new snow parametrization. *Monthly Weather Review*, *136*, 5095. https://doi.org/10.175/2008MWR2387.1

van Wessem, J. M., van de Berg, W. J., Noël, B. P. Y., van Meijgaard, E., Amory, C., Birnbaum, G., et al. (2018). Modelling the climate and surface mass balance of polar ice sheets using RACMO2: Part 2: Antarctica (1979–2016). *The Cryosphere*, *12*(4), 1479–1498. https://doi.org/10.5194/tc-12-1479-2018

Vaughan, M. A., Young, S. A., Winker, D. M., Powell, K. A., Omar, A. H., Liu, Z., et al. (2004). Fully automated analysis of space-based lidar data: An overview of the CALIPSO retrieval algorithms and data products. In *Proc.SPIE, 5575*. https://doi.org/10.1117/12.572024

Vignon, E., Hourdin, F., Genthon, C., Van de Wiel, B. J. H., Gallée, H., Madeleine, J.-B., & Beaumet, J. (2018). Modeling the dynamics of the atmospheric boundary layer over the Antarctic Plateau with a general circulation model. *Journal of Advances in Model Earth Systems*, *10*, 98–125. https://doi.org/10.1002/2017MS001184

Vignon, É., Traullé, O., & Berne, A. (2019). On the fine vertical structure of the low troposphere over the coastal margins of East Antarctica. *Atmospheric Chemistry and Physics*, *19*(7), 4659–4683. https://doi.org/10.5194/acp-19-4659-2019

Wang, Y., Ding, M., van Wessem, J. M., Schlosser, E., Altnau, S., van den Broeke, M. R., et al. (2016). A comparison of antarctic ice sheet surface mass balance from atmospheric climate models and in situ observations. *Journal of Climate*, *29*(14), 5317–5337. https://doi.org/10.1175/JCLI-D-15-0642.1

Young, G., Lachlan-Cope, T., O'Shea, S. J., Dearden, C., Listowski, C., Bower, K. N., et al. (2019). Radiative effects of secondary ice enhancement in coastal antarctic clouds. *Geophysical Research Letters*, *46*, 2312–2321. https://doi.org/10.1029/2018GL080551

Yuter, S. E., & Houze, R. A. (1995). Three-dimensional kinematic and microphysical evolution of Florida cumulonimbus. Part II: Frequency distributions of vertical velocity, reflectivity, and differential reflectivity. *Monthly Weather Review*, *123*(7), 1941–1963. https://doi.org/10.1175/1520-0493(1995)123<1941:TDKAME>2.0.CO;2